Computations of energetic nearshore waves: Are weakly dispersive phase-resolving models telling the same story?

Assaf Azouri, Volker Roeber, Martin D Guiles, Mark Merrifield, Janet Becker, Douglas S Luther

Coastal Engineering 194 (2024) 104625

Contents lists available at ScienceDirect

Coastal Engineering

journal homepage: www.elsevier.com/locate/coastaleng

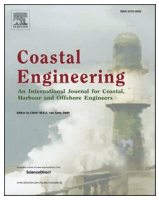

Computations of energetic nearshore waves: Are weakly dispersive phase-resolving models telling the same story?

Assaf Azouri [a,*], Volker Roeber [b,a], Martin D. Guiles [a,1], Mark Merrifield [c], Janet Becker [c], Douglas S. Luther [a]

[a] University of Hawai'i at Mānoa, Department of Oceanography, School of Ocean and Earth Science and Technology (SOEST), Honolulu, Hawai'i, 96822, USA
[b] Université de Pau et des Pays de l'Adour, E2S UPPA, SIAME, 64600, Anglet, France
[c] Scripps Institution of Oceanography, La Jolla, CA, USA

ARTICLE INFO

Keywords:
Phase-resolving models
Boussinesq
Non-hydrostatic
Infragravity
High-energy swell
Wave transformation

ABSTRACT

Three phase-resolving weakly dispersive wave models are used for 2DH (2D depth-integrated) computations of large-scale wave-by-wave processes induced by highly energetic sea/swell (SS) forcing near Haleʻiwa on the North Shore of Oʻahu, Hawaiʻi. The computed model results are compared to observations obtained over a nearshore cross-reef transect and from the basin of a small boat harbor. The level of agreement between the model results and observations in complex coastal environments under highly energetic wave forcing, along with the qualitative consistency among the three models, makes these models good candidates for operational applications in nearshore environments exposed to energetic wave forcing conditions.

Spectral analyses inside the harbor and over the reef indicate that all three models generally account for infragravity (IG) spatial modal structures that are consistent with observations and the theory of edge and leaky waves. Over the reef, auto- and cross-spectral analyses reveal that the dominant waveforms are qualitatively reproduced by all three models, as indicated through: (i) the growth of IG wave amplitudes from deeper water to the shallow reef sites; (ii) the agreement of power spectral density peaks at the nearshore locations; and (iii) the remarkable similarity of spatial coherence functions among the models and between the models and observations. The computations of swell entering the small boat harbor at Haleʻiwa demonstrate that the models can successfully reproduce the variability in the narrow IG frequency bands that are spatially dependent and often subject to resonant amplifications.

1. Introduction

To adequately address coastal risks such as wave-driven run-up and flooding, many researchers have been turning to use powerful numerical models that can resolve various wave processes, such as: refraction, diffraction, and wave-wave interactions. Phase-resolving models are becoming a popular choice for many applications, though their use in one-dimensional mode along a cross-shore transect is still common practice to minimize computation times. As part of the recent development of wave-driven run-up and flood mapping products for a large stretch of coastline in Hawaiʻi, a phase-resolving model (BOSZ; Roeber and Cheung, 2012) was used in two-dimensional mode under highly energetic incident wave conditions over a large computational domain. Since there are other phase-resolving models in use by the scientific and engineering communities, it was decided to assess the BOSZ model against two of the most commonly used phase-resolving models: FUNWAVE (Shi et al., 2012) and XBeach-NH (Roelvink et al., 2009), and examine the performance of the three models against each other and against observations. Even though these models share many similarities, it is not guaranteed to the user that they will produce results that are

* Corresponding author.
E-mail addresses: assaf@hawaii.edu (A. Azouri), volker.roeber@univ-pau.fr (V. Roeber), mamerrifield@ucsd.edu (M. Merrifield), jmbecker@ucsd.edu (J. Becker), dluther@hawaii.edu (D.S. Luther).

[1] Dr. Martin D. Guiles passed away in July, 2023, before completion of this paper. His contributions to it were fundamental, but, more importantly, his contributions, usually unheralded, to the projects of numerous students and colleagues in the School of Ocean and Earth Science and Technology at UH, promoted excellence and collegiality that are already broadly missed. He was a person with an insatiable curiosity of physical phenomena, technology and digital tools. His nature was joyful and his laugh infectious. His heart was filled with love for, and support from, his wife and three daughters, who have survived him.

https://doi.org/10.1016/j.coastaleng.2024.104625
Received 19 January 2024; Received in revised form 22 September 2024; Accepted 23 September 2024
Available online 26 September 2024

consistent with realistic ocean observations. Furthermore, there are not many studies that have used these models under very high wave amplitude conditions.

In recent decades, numerous phase-resolving models were developed and became available to the community. Some are commercially marketed (e.g., MIKE21), while others are available as open source or distributed among a user community (e.g., XBeach, BOSZ, FUNWAVE, SWASH, REEF3D). Although these models may vary in their formulations and governing equations - some are non-hydrostatic, whereas others are of Boussinesq-type - they all keep track of the evolution of individual waves and the relative phases among them, and resolve the evolution of infragravity (IG) wave fields as secondary processes via non-linear triad interactions and wave breaking.

The three phase-resolving models that are examined here: XBeach-NH, FUNWAVE, and BOSZ, have been used previously in multiple studies and application-oriented projects before and have led to scientifically valid results as documented in various publications. These models share several common features such as the fundamental subset of Shallow Water Equations, wet–dry moving boundaries, as well as a wave generation mechanism that depends on the superposition of individual monochromatic waves with a random phase.

The Xbeach model is well-known and is mostly applied in its classic "surfbeat" mode (Roelvink et al., 2009), where the wave input is the envelope of the wave group rather than the full free-surface timeseries of irregular waves. Xbeach-NH (Smit et al., 2010) is a phase-resolving, depth-integrated non-hydrostatic model, which obtains its non-hydrostatic pressure correction from an approximation of the vertical velocity. This model is therefore similar to a one-layer version of the SWASH model (Zijlema et al., 2011) or to the well-established tsunami model NEOWAVE (Yamazaki et al., 2011). Xbeach-NH has been mainly used for wave runup and its associated sediment transport (e.g. Roelvink et al., 2018; Mancini et al., 2021; Elsayed et al., 2022). Recent applications also include wave patterns from ship wakes (Almström et al., 2021). Xbeach-NH+ (de Ridder et al., 2021) is a recent extension of Xbeach-NH, with slightly improved dispersion properties; however, due to the recent development, the standard Xbeach-NH code is used in this study.

FUNWAVE-TVD is a phase-resolving, depth-integrated Boussinesq-type model based on the governing equations from Chen, (2006) - an extension of the more basic set of equations by Nwogu (1993), which is also an option in the model. FUNWAVE-TVD uses the conservative form of the governing equations and benefits from MPI parallelization. The model has been extensively applied to explain nearshore wave characteristics. The model has served to analyze various tsunami-related processes (see Grilli et al., 2015a; Grilli et al., 2015b; Shelby et al., 2016; Schnyder et al., 2016) and longshore currents at open beaches (Choi et al., 2015). The model was extended to handle ship-born waves in waterways (Shi et al., 2018; Malej et al., 2019) and sediment transport under tsunamis (Tehranirad et al., 2016). Recent efforts by Su and Ma (2018), and Su et al. (2021), show that the model is able to reproduce IG wave motion over a complex reef.

The BOSZ numerical modeling tool (Roeber et al., 2010; Roeber and Cheung, 2012b) is a phase-resolving, depth-integrated, Boussinesq-type model based on the set of equations from Nwogu (1993), though expressed in conservative form. The numerical scheme offers two options for the hydrostatic part of the equation: the classic HLL Riemann solver or a second-order upwind flux scheme, whereas the dispersion terms are solved with a second-order central Finite Difference scheme. Previous studies using BOSZ include tsunamis and long waves (Horillo et al., 2015; Lynett et al., 2017; Roeber and Cheung, 2012a; Morichon et al., 2021), harbor oscillations (Azouri et al., 2018; Bellafont et al., 2018), nearshore wave transformations (Li et al., 2014; Filipot et al., 2019; Varing et al., 2021; David et al., 2021), high-resolution wave run-up (Pinault et al., 2020, 2022; Kalisch et al., 2023) and extreme IG-waves (Roeber and Bricker, 2015). The model has also been extended with transport equations for boulders and sediment and successfully applied to reconstruct past catastrophic events (see Watanabe et al., 2021; Watanabe et al., 2022). Additional source terms are available to account for the effects of ship-borne waves (David et al., 2017). Recently, the model was employed for an investigation of dependencies of vortex patterns in the surf zone (Bondehagen et al., 2024).

The user's preference to utilize a particular model depends on the applicability of the model to a site-specific hydrodynamic problem. The advantage of using phase-resolving models for nearshore wave processes (as opposed to spectral models) is that they resolve the interaction of multiple single waves among each other and with the bathymetry. This results in energy transfer processes between gravity and IG waves leading to a realistic representation of the nearshore wave field including run-up and circulation.

Although inter-model comparison studies have been conducted in the coastal engineering community (e.g., Gruwez et al., 2020; Lashley et al., 2020), the studies were mostly carried out with models of different types (e.g. 3D vs. 2DH vs. spectral) and for problems involving wave structure interactions.

In this study, three depth-integrated models of similar applicability are investigated for their level of consistency with respect to nearshore wave processes, excluding run-up and overtopping. Hereby, the performance of these models is tested using large 2D domains in combination with energetic sea/swell (SS) forcing conditions in two types of systems several kilometers apart: (i) a fringing reef; and (ii) a harbor. Energetic SS forcing events trigger a response at all IG frequencies (e.g., see Figures 2.12-2.14 in Azouri, 2016). Forcing the models with such energetic input allows for analyses of the underlying physics, as it pushes the models to generate large amplitude responses from nonlinear interactions. Over the fringing reef, the strong response at IG frequencies can lead to a broad range of IG wavenumbers (e.g., for edge waves, several wavenumbers can exist for a given frequency). In the harbor, which is an enclosed basin, we expect to see specific structures with particular frequencies that correspond to the normal modes of the basin (e.g., see Figure 2.9 in Azouri, 2016). Also, during time periods of strong SS forcing the observed coastal response has energetics that exceeds responses from other possible sources. This is important, since in the ocean other sources of energy, such as internal waves, open ocean IG waves, etc., could complicate the interpretation of the results. With strong enough SS, the energy and associated spectral signatures of these alternative sources may be ignored.

The response of the harbor and the coast to varying levels of SS forcing amplitudes was studied by Azouri (2016) (e.g., see figures 2.7 and 2.12-2.14). This study revealed that naturally resonant modes in this domain (harbor or coastal) are more apparent under weak SS forcing amplitudes, whereas strong SS forcing levels push a broad IG band to high amplitudes and the character of the response is a saturated spectrum without specific resonant frequencies. The exception is the response of the 1–6 min IG band inside the harbor that retains its modal character in a wide range of SS forcing conditions.

Analyses of the model outputs from the present study are compared with data collected from sites on the North Shore of O'ahu. The models were set up in the most consistent way possible, i.e., identical boundary conditions such as the bathymetry grid, wave spectra, friction, etc., to ensure that any discrepancies we find can be attributed to differences of the dynamics rendered among the models.

2. Model setup

The two main boundary conditions that these models require are: (i) bathymetry and topography datasets (preferably of high resolution); and (ii) a directional spectra for the wavemaker.

2.1. Computational grids and domains

The main results presented here are from simulations using a 12.2 km (alongshore) x 10.2 km (cross-shore) domain (hereafter, called the

large domain) stretching from Mokuleia to Laniakea, with a grid resolution of 7 m × 7 m (see Fig. 1). This particular grid resolution is a compromise between sufficiently high resolution to achieve converging results - especially in narrow parts of Hale'iwa Harbor that are on the order of tens of meters - and the need for a reasonable turnaround time of the computations given the suite of runs necessary and the computational resources available. Additional testing of coarser and finer grid resolutions was done by Tognacchini (2022).

Additional scenarios are described in the sensitivity analysis of section 4. Details about the wave events that were simulated, their wave statistics, and the corresponding modeling setup, are provided in Table 1. Tide levels were obtained from Hale'iwa Harbor tide gauge. The results from the additional modeling scenarios are shown for one model at selected representative sites.

2.2. Boundary conditions

2.2.1. Bottom boundary: bathymetry/topography

Three different datasets were blended to create bathy/topo files for the model domains. The datasets are: (i) 50 m resolution Multibeam, for the offshore region (collected by the Hawai'i Mapping Research Group; http://www.soest.hawaii.edu/HMRG/multibeam/index.php); (ii) 5 m resolution Lidar for the coastal region (from USACE's 2013 survey; https://coast.noaa.gov/dataviewer/#/); and (iii) 3 m resolution hydrosound for Hale'iwa Harbor (Portland District Corps of Engineers, 2009). The maximum depth was set to 80 m.

2.2.2. Side boundaries

In the XBeach (XB) model, a weakly-reflective wave and flow condition is imposed to minimize reflections from the offshore boundary, and Neumann condition (setting the longshore gradient to zero) at the lateral boundaries (Roelvink et al., 2009). In BOSZ (BZ) and FUNWAVE (FW), a sponge layer is applied at all open ocean boundaries (offshore and lateral; Larsen and Dancy, 1983). The sponge layer damps out the amplitude of outgoing waves, therefore minimizing the potential of wave reflections from the domain boundaries. BOSZ takes the peak wavelength as reference for the width of the sponge layer. For instance, for a 15 s wave (having a wavelength of ~330 m at 80 m depth), the sponge layer will extend over approximately 48 cells in the cross-shore. It is worth noting that the width of the sponge layer is not absolutely critical; reasonable absorption can be achieved even with a small number of cells (Larsen and Dancy, 1983).

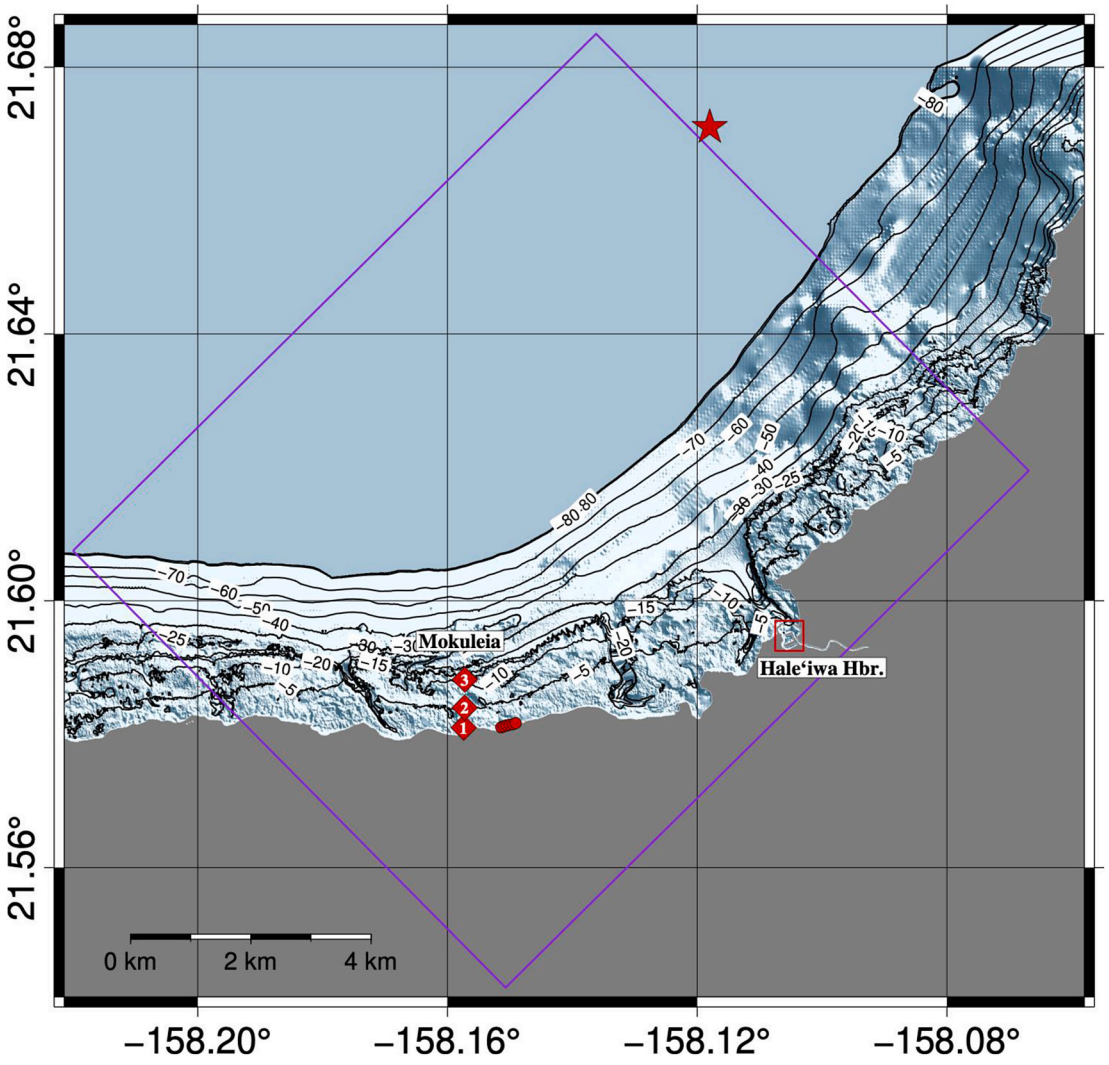

Fig. 1. Bathymetry map including the boundaries of our computational domain on the north shore of O'ahu Island, Hawai'i. The red star indicates the location of the Waimea Buoy, where the directional input spectra for the models were taken from. The red diamond symbols indicate locations where observational data were available over the reef at Mokuleia (1–3 correspond to Mok1-Mok3 sites in the text), and the nearby red circles are the locations of our alongshore virtual array. Locations of sea level observations from Hale'iwa Harbor are shown in the following figure. This domain was used for simulations 1–4 (see Table 1) of all three models.

Table 1
Summary of the wave statistics used for the events that were simulated with their corresponding model parameters. From left to right, the columns are: (i) simulation #; (ii) time from the center of the window for the directional spectra file that was used as input to the models; (iii) duration of the model run; (iv) alongshore and cross-shore extent of the computational domain; (v) resolution of the bathymetry grid; (vi) significant wave height of the swell event; (vii) peak period of the swell event; (viii) peak direction of the swell event; and (ix) the mean tide level for Hale'iwa Harbor location (obtained from Hale'iwa Harbor tide gauge) at the center of the 4-h simulation window. In all simulations with the three models we use $kh = \pi$ as a condition to limit the shortest waves included in the input to the models.

Simulation	Event [GMT]	Simulation Duration [hr]	Domain [km x km]	Grid Res [m x m]	Hs [m]	Tp [sec]	Dp [deg]	Mean Tide Level [m]
1	2014/01/23, 06:55	4	12.2 × 10.2	7 × 7	7.4	15.4	315	0.04
2	2008/01/13, 22:40	4	12.2 × 10.2	7 × 7	6.1	18.2	310	−0.13
3	2008/01/13, 22:40	4	12.2 × 10.2	14 × 14	6.1	18.2	310	−0.13
4	2008/01/13, 22:40	4	12.2 × 10.2	21 × 21	6.1	18.2	310	−0.13
5	2014/01/23, 06:55	4	1.9 × 3.9	7 × 7	7.4	15.4	315	0.04

2.3. Wavemaker

For a given simulation, all three models are forced with a directional spectra near the offshore-most boundary of the domain in 80 m depth. The directional spectra for the Waimea Buoy (North Shore of O'ahu, Hawai'i) are obtained from PacIOOS Waimea Datawell Directional Waverider Mark III buoy (Coastal Data Information Program CDIP, McManus et al., 2001), for two highly energetic SS forcing events, during which bottom pressure records were available over the reef or inside Hale'iwa Harbor. These events are: (i) January 13, 2008 ($H_{s,max} = 6.1\ m$, $T_p = 18.2$ s, $D_p = 310\ deg$), during which data was available at the three reef sites in Mokuleia,;and (ii) January 23, 2014 ($H_{s,max} = 7.4\ m$, $T_p = 15.4$ s, $D_p = 315\ deg$), during which data was available at several sites inside Hale'iwa Harbor.

Since the governing equations in most phase-resolving models apply to long and intermediate waves, it is advisable to avoid the generation of short input waves. As a safe guideline, the shortest generated input wave should not exceed $kh = \pi$ (i.e., $L\ min = 2h$). Shorter input waves would be subject to progressively larger errors in phase speed. In the present case with a maximum depth of 80 m in the bathymetry grid, the frequencies that correspond to wavelengths shorter than 160 m are excluded from the original directional spectrum input and the energy corresponding to the high frequency tail of the spectrum is redistributed over the remaining frequency bins (Roeber et al., 2019). From linear wave theory, the resulting frequency cutoff is about 0.1 Hz (or, T = 10 s). With peak periods of the two swells corresponding to 18.2 s and 15.4 s, only little energy remains in frequencies above 0.1 Hz; therefore the overall spectral shape is maintained, which is necessary to preserve the fundamental properties of the swells such as wave group formation and subsequent shoaling and refraction processes.

All of the results presented here are based on the computed wave fields from a 4-hr time series. Though the input wave spectrum remains constant and a saturated wave field is noticeable after 20–30 min, long computations allow for accurate modeling of longer IG period waves (T > 10 min). Additionally, longer periods of computations provide larger windows for the coherence analysis. The first half hour of the computation is allocated for the development of a saturated sea state and therefore excluded from the data analyses. The input wave spectrum obtained from the CDIP buoy contains a bi-linear frequency binning of df = 0.005 Hz below 0.1 Hz and df = 0.01 Hz above the frequency of 0.1 Hz. With each frequency bin representing a linear wave with a random phase, a time series from all waves in the spectrum would recycle after 1/(0.005 Hz), i.e. after 200 s. This process would lead to artificial wave groups and false representation of IG-waves nearshore. It is therefore important to redefine the spectral binning according to the computed time span so that all individual waves generated by the wavemaker interact once with each other during the computation and no recycling occurs. A 4-hr computed time consequently requires a very small frequency binning of df = 1/(4 hr) = 0.00007 Hz. With the lowest frequency of the wave spectrum at 0.025 Hz and the truncation of the high frequency tail at 0.1 Hz, the remaining spectrum is divided into 1072 uniformly-spaced frequency bins. The directional window was limited to 40 deg on either side of the peak direction with a directional binning of 2 deg. The interpolated input spectrum is consequently composed of 43952 individual wave components (1072 frequency bins and 41 directional bins) each with a pre-assigned random phase. The seed for the random phase distribution was kept constant to ensure repeatability of the computations.

This preprocessing technique is not part of the FUNWAVE code. Therefore, the pre-processed input from BOSZ was directly used in FUNWAVE to ensure consistency in the computations. In XBeach, the pre-processing stage is done internally and cannot be controlled by the user. Coincidentally, the XBeach model relies on a hard-coded truncation of the shortest input wave at $kh = \pi$, which lead to the same frequency range as in FUNWAVE and BOSZ. However, the phase distribution is likely different. Though it was shown by Roeber and Bricker (2015) and Pinault et al. (2020) that the phase seeding can have an impact on run-up and overtopping, the wave phases usually do not significantly affect the overall wave field as long as the solution is obtained over a sufficiently long period of time, implying that the wavemaker generates a large number of individual waves. The more a time series is composed of many waves, the less a single wave contributes to the overall spectral composition and integrated properties such as wave set-up.

2.4. Friction

Friction is enabled in all three models in terms of the Manning Roughness coefficient, using a constant value of $n = 0.035\ sm^{-1/3}$, a value that was experimentally determined to be representative for the lava reef bottom commonly found in Hawai'i (Bretschneider et al., 1986). Numerous studies have used this particular value in Hawai'i and confirmed that this coefficient value represents the volcanic reef environment as the one found on the North Shore of O'ahu, Hawai'i (e.g., Roeber and Cheung, 2012b; Cheung et al., 2013).

2.5. Limitations

It is important to acknowledge that the Waimea Buoy, which provides the source for the input spectrum of the wavemaker in the respective models, is located just outside the model domain, and its data is recorded at a water depth of 200 m. In contrast, the offshore water depth in the model grid is limited to 80 m to avoid violating the dispersion properties inherent in the models, as discussed earlier. These issues were identified early in the validation process, and carefully assessed in terms of their impact on the computed results.

At the Waimea Buoy's depth of 200 m, incoming swell undergoes minimal shoaling. According to linear wave theory, for a wave with a peak period of 18 s, the shoaling coefficient is approximately 0.975. This value reflects the fact that the shoaling coefficient initially drops below unity before increasing rapidly in shallower waters. At 80 m depth, however, the shoaling coefficient is 0.913. The input spectra therefore do not fully account for the shoaling effect between 200 m and 80 m depth, which in turn has the effect of a slightly exaggerated input wave field. Preliminary tests that reduced the overall spectral energy by 8–9% produced closer agreement with the observed data across all models.

We also explored the use of a spatially-varying suite of input spectra, however, this feature was unavailable in the version of FUNWAVE used for this study. As part of the investigation of the sensitivity of the results on the wave input, we recalculated one of the swell scenarios using the spectral models WaveWATCH III and SWAN, and extracted an array of spectra along the offshore boundary of the model domain to obtain spatially varying input spectra. The wavefield in both 200 m and 80 m depth was relatively homogeneous, and no significant improvement was observed at the pressure sensor locations that could have been attributed to small spatial variations in the composition of the input spectra.

Despite these findings, this study intentionally refrains from adjusting the input spectrum or utilizing auxiliary models, as these measures would introduce additional uncertainty. In practice, an ideal input spectrum is often unavailable. The objective here is not to fine-tune parameters to achieve the closest possible match to the observed data, but rather to demonstrate how the selected suite of models performs as an ensemble under commonly encountered constraints and to provide a broader understanding of what can be reasonably expected from this family of models under realistic conditions. By prioritizing robustness and general applicability over precision through questionable parameter adjustment, the results below offer insights that are more broadly applicable to the modeling community.

3. Datasets & analysis methods

3.1. Datasets

Bottom mounted pressure sensors were deployed in a cross-shore transect at Mokuleia reef during the 2007–2008 winter swell season. The sensors sampled at 1 Hz and the free-surface elevation estimates were obtained from the pressure records using linear wave theory (the data were collected by M. Merrifield and J. Becker; quality assessment was provided by Azouri, 2016). The deployment sensor depths were 2 m, 6 m, and 12 m (see sites 1-3 in Fig. 1) respectively. The Mokuleia raw pressure data and the free-surface elevation estimates from January 13, 2008 used in this study can be provided upon request. For the harbor, we use bottom pressure records that were collected at several locations inside the harbor (data records between Nov 28, 2013 and May 22, 2014; Azouri, 2016). Results for harbor sites 1 & 4 are shown here, and their location inside the harbor is shown in Fig. 2. The sampling period in the harbor was different at each site, ranging from 3 s to 14 s, with different averaging intervals in between samples. For the numerical

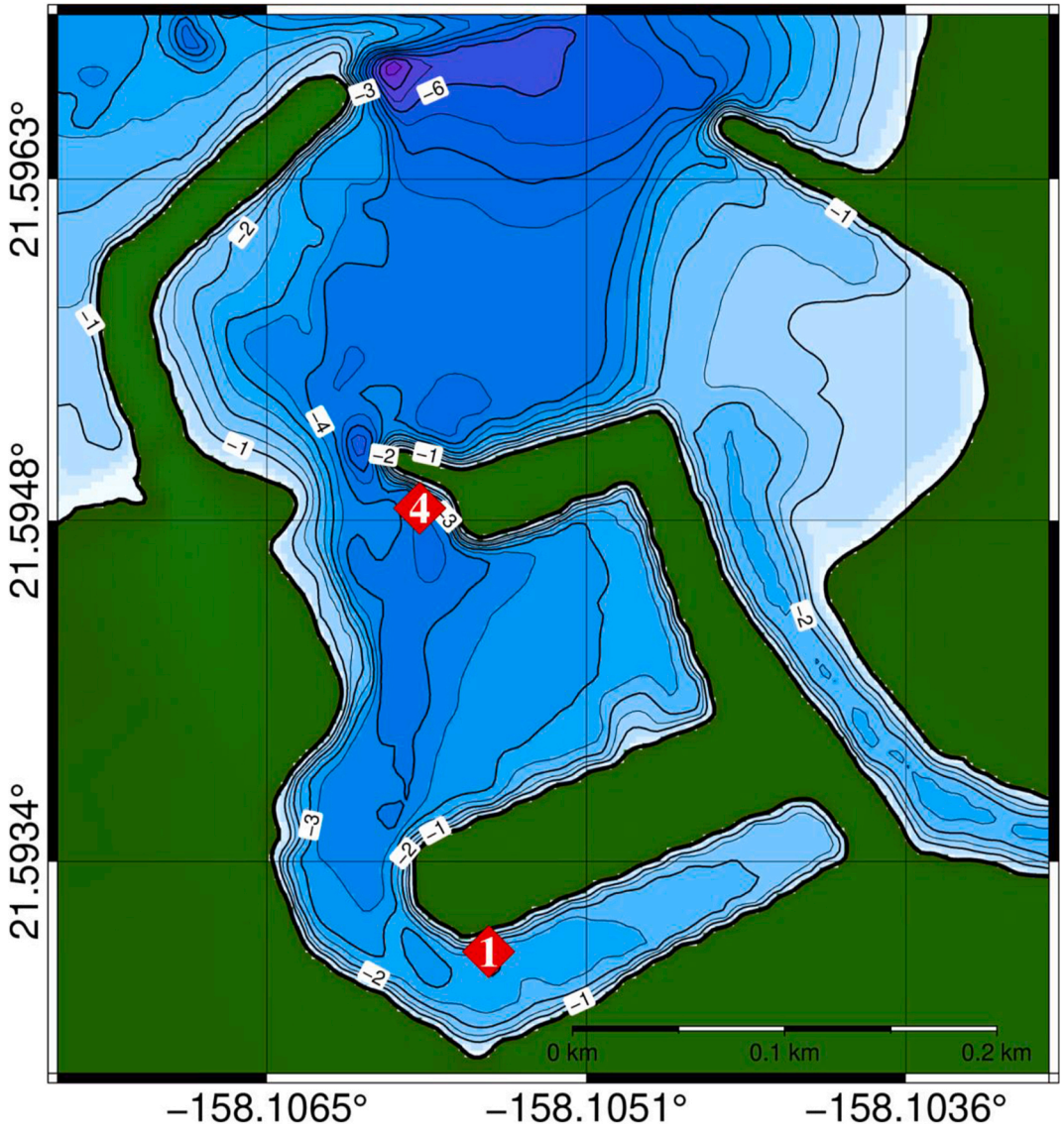

Fig. 2. Bathymetry map of Hale'iwa Harbor. Red diamond symbols indicate sites Hale1 and Hale4 where sea level observations were available. Depth contours are plotted at 0.5 m intervals.

model outputs, at each of the above observational sites we placed virtual gauges in the models and sampled the free surface output at 1 Hz. Model output was also recorded from six sites forming a 550 m-long alongshore array positioned 30 m from shore and centered ~900 m east from the observational Mokuleia cross-shore array. Edge waves, which appear to dominate the nearshore IG wavefield, have a nearshore maxima and for most of the period bands a distance of 30 m from shore captures their maxima (Azouri, 2016).

In comparing the modeled and observed results below we used observations from 2-hr before until 2-hr after the observation time of the spectra that were fed into the wavemakers of the three models. Over that 4-hr period of time, the significant wave height (Sabatier, 2007; part 2, chapter 1), peak period, and peak direction remained within 15%, 1 s, and 10 deg of the values, respectively, observed at the peaks of the events (Table 1).

3.2. Analysis methods

Auto- and cross-spectral calculations are implemented to generate plots of power spectral density (PSD) and coherence (amplitude and phase), respectively.

The auto-spectral analysis provides useful information about the ability of the models to generate a wave field with the proper energy levels as a function of frequency. A cross-spectral analysis can further provide insight into the ability of the models in generating the proper wavenumbers (or, wavelengths) as a function of frequency. The coherence amplitude and coherence phase functions are calculated for a given pair of sites (with a corresponding fixed distance); for a coherent signal, the coherence phase will allow us to determine what length scales correspond to the underlying wave signals.

The PSD is calculated following the frequency averaging method (equation (1)), as described in Thomson and Emery (2014), with the exception that we increase the number of spectral estimates within the frequency bands as we go to higher frequencies; this results in relatively uniform visualization of the spectra across the entire logarithmic frequency range of a given dataset, and decreasing confidence intervals going to high frequencies (since the number of degrees of freedom increases).

$$S_{xx}(f) = 2\frac{|\mathrm{X}(f)|^2}{df}, \tag{1}$$

where $\mathrm{X}(f)$ is the Fourier transform of the windowed time series, $df = \frac{1}{N*dt}$ is the frequency spacing, N is the record length, and dt is the sampling period.

The PSD is normalized so that the variance of a unit amplitude sine wave is ½, and the 95% confidence intervals for independent spectrum estimates are calculated following Thomson and Emery (2014).

The cross-spectra, $S_{xy}(f)$, is calculated following Thomson and Emery (2014):

$$S_{xy}(f) = 2\frac{X(f)Y(f)}{df}, \tag{2}$$

and together with the auto-spectra, these are then used to calculate the coherence amplitude, $\gamma(f)$, and coherence phase, $\varnothing(f)$ functions (equations (3) and (4)):

$$\gamma(f) = \sqrt{\frac{S_{xy}(f)^* S_{xy}(f)}{S_{xx}(f)S_{yy}(f)}}, \tag{3}$$

$$\varnothing(f) = \arctan\left[\frac{im(S_{xy}(f))}{re(S_{xy}(f))}\right]. \tag{4}$$

For the coherence amplitude function, the 95% level of no significance is calculated following Thompson (1979).

The sign convention used here for the coherence phase function implies that the signal at site b is leading the signal at site a for a positive phase difference between sites a and b. All auto- and cross-spectral estimates are calculated by applying 50% overlap between adjacent spectral estimates. To minimize spectral leakage, we apply a 10% cosine-taper Tukey window, as described in Thomson and Emery (2014).

4. Sensitivity analysis

Using the auto-spectral techniques that were described above, we look at the sensitivity of the numerical models to different grid resolutions, and a different domain size. Here we show results from the BOSZ model, which are qualitatively representative for all three models.

4.1. Grid resolution

In addition to the results from simulations using the 7 m × 7 m grid, we tested the sensitivity of the results for two coarser grid resolutions: 14 m × 14 m and 21 m × 21 m (see simulations 3 and 4 in Table 1). Though these coarser resolutions are not the preferred options for computations, the fast turnaround time can be of advantage for first estimates as long as the numerical solutions are representative. The results, as seen in Figure S1 for Mok1 site, reveal that the spectra derived from the output computed with the highest spatial resolution (blue curve) have the best definition of the spectral peaks and valleys when compared to the observations (e.g., at 30 s, ~80 s, and ~8 min), and they also have the most representative spectral amplitudes at the high frequency SS band (e.g., down to ~10 s). The spectra of the coarser resolution grids qualitatively resemble the one of the 7 m × 7 m grid, but they severely underestimate the spectral amplitudes at the high frequency regime of the SS band, and overestimate them by up to an order of magnitude at periods longer than 2 min.

4.2. Domain sizes

We also looked at spectra from harbor site Hale1 using sea level data that was obtained from model simulations over a 7 m × 7 m grid and from a smaller domain (simulation 5 from Table 1; here referred to as the "small domain") than the one used throughout this study (simulation 1 from Table 1; here referred to as the "large domain"). The extent of the small domain is 1.9 km in the alongshore (centered on Hale'iwa Harbor) and 3.9 km in the cross-shore. Figure S2 provides a comparison of the spectra from those simulations, and the spectra that were calculated from the corresponding sea level observations. Although the two spectral curves of the model (blue and orange) follow the shape of the spectra from observations, we find better agreement between the spectra of the large domain (blue curve) and observations, especially at periods shorter than 40 s, and in the 3–12 min period band.

5. Results

5.1. Models versus observations: comparison

Auto-spectral techniques were used to test the capability of the models to reproduce observed frequency responses in the confined basins of the harbor (see section 3.2 for details about the spectral techniques), and along the coast over the Mokuleia reef. This is complemented by applying a cross-spectral analysis to reveal information about the wavenumber content generated by the models. Inside the harbor, we test the models' capability to reproduce the observed spatial structure of the modes, which is unique to the harbor. At the observational sites of the Mokuleia reef we look at the coherences in the cross-shore direction and compare these to the observations. At Mokuleia, we also used model outputs from an alongshore array, and implemented the Iterative Maximum Likelihood Estimate (IMLE) following Oltman-Shay and Guza (1987). Although observations are not available along this

array, this analysis is another useful tool for highlighting potential consistency among the models in reproducing the wavenumber content over the reef. This tool is also particularly useful in identifying the signature of IG edge waves, as these have unique discrete dispersion relation curves.

5.1.1. Spectra inside the harbor

The model outputs discussed here correspond to simulation 1 from Table 1. As is shown in Figs. 3 and 4, the spectra generated from the bottom pressure observations (black curves) reveal the unique spectral peaks and valleys at Hale1 and Hale4 sites, which reflect the complex spatial distribution of the dominant modes in the harbor (the spectra at two additional sites inside the harbor can be found in Azouri, 2016, Figure 2.9). The corresponding spectra generated from outputs of the three models (blue, red, and orange curves) reveal a structure that is consistent with the spectra of the bottom pressure observations. The major peaks and valleys of the model curves appear at frequencies that are consistent with the corresponding observations, especially in the IG period band of 30 s to 4–5 min. Around 2–3 min and at periods longer than ~5 min, some of the models appear to overestimate the spectral amplitudes by as much as an order of magnitude.

Fig. 5 shows the coherence amplitude and coherence phase between harbor sites Hale1 and Hale4. The overall structure of the coherence functions created from the model outputs is consistent with the structure of the corresponding curves from observations. The coherence amplitude in all three models decreases sharply around certain periods (5–6 min, 2–3 min, and 60–70 s), with corresponding jumps of ~180 deg in coherence phase and stable phase values in between those dips. That is a signature of resonant motions, when a node exists between two sites. The periods where the sharp transitions in coherence amplitude and phase occur are remarkably close to the observed periods. Figs. 3 and 4 reveal a series of spectral peaks at Hale1 and Hale4 sites. A more detailed analysis of the modes in that harbor using lengthy data records was done by Azouri (2016), indicating the 3 min and 6 min as the two gravest modes of this harbor.

5.1.2. Spectra over the reef

The Mokuleia fringing reef model comparisons correspond to simulation 2 from Table 1. In Figs. 6–8 we see that at the offshore site (Mok3, 12 m depth) the observed spectra (black curve) is broad-banded and mostly white, with a clear dominant peak in the SS band (18 s). As the waves propagate through the surf zone (Mok2, 6 m depth; Mok1, 2 m depth), energy is lost at SS periods and new broad-banded peaks and valleys appear at IG periods.

At the offshore site (Mok3, 12 depth; Fig. 6), all models reproduce the observed peak period and spectral amplitude of the 18 s SS peak. In the 0.5–15 min band, the overall spectral levels of the models are within an order of magnitude of the observations.

At the intermediate depth site (Mok2, 6 m depth; Fig. 7), the spectra from the models are resolving the broad-banded peaks at the observed SS and IG periods: ~18 s, ~90 s, ~3–4 min, and ~12 min. However, the corresponding spectral amplitudes of the models at those peaks are over- or under-estimated by up to nearly an order of magnitude, and the statistical certainty of the IG peaks is low. In the period range of 20-60 s, XB and BZ overestimate the observed spectral amplitudes. At periods shorter than the peak swell period, FW underestimates the spectral amplitudes, and the spectral amplitudes in XB and BZ are able to reproduce the observed spectra. At the high frequency regime of the SS band we find that the spectral amplitudes of XB and BZ over the reef are qualitatively more representative of the corresponding spectra from observations than the spectral amplitudes of FW. The power spectral density (PSD) of the FW curve is an order of magnitude or more lower than the observations whereas XB and BZ are within half an order of magnitude of the observations.

At the nearshore site (Mok1, 2 m depth; Fig. 8), the observed spectrum contains several peaks centered on the IG periods: ~50 s, ~5 min,

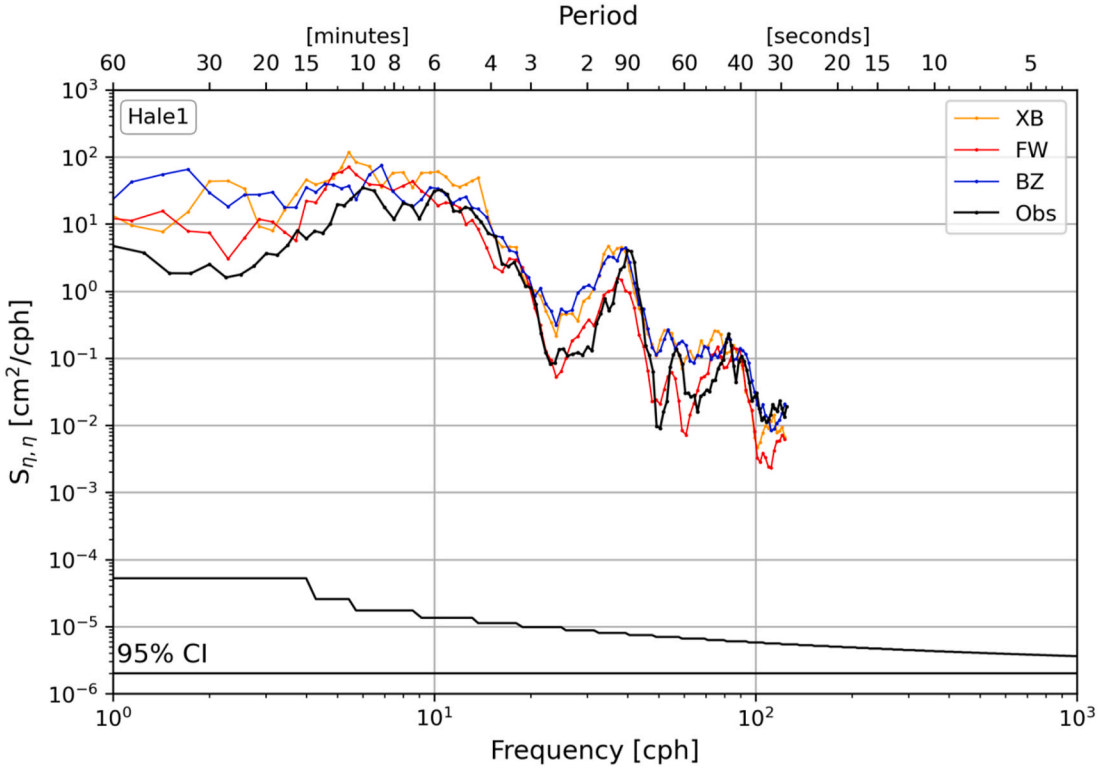

Fig. 3. Power spectral density of observed sea level (black curve), and modeled sea level (BZ, blue curve; FW, red curve; XB, orange curve) at harbor site Hale1. The model records are from simulations using a 7 m × 7 m grid (simulation 1 in Table 1). The vertical distance between the black lines at the bottom represents the 95% confidence interval for independent spectrum estimates. Every other point is independent.

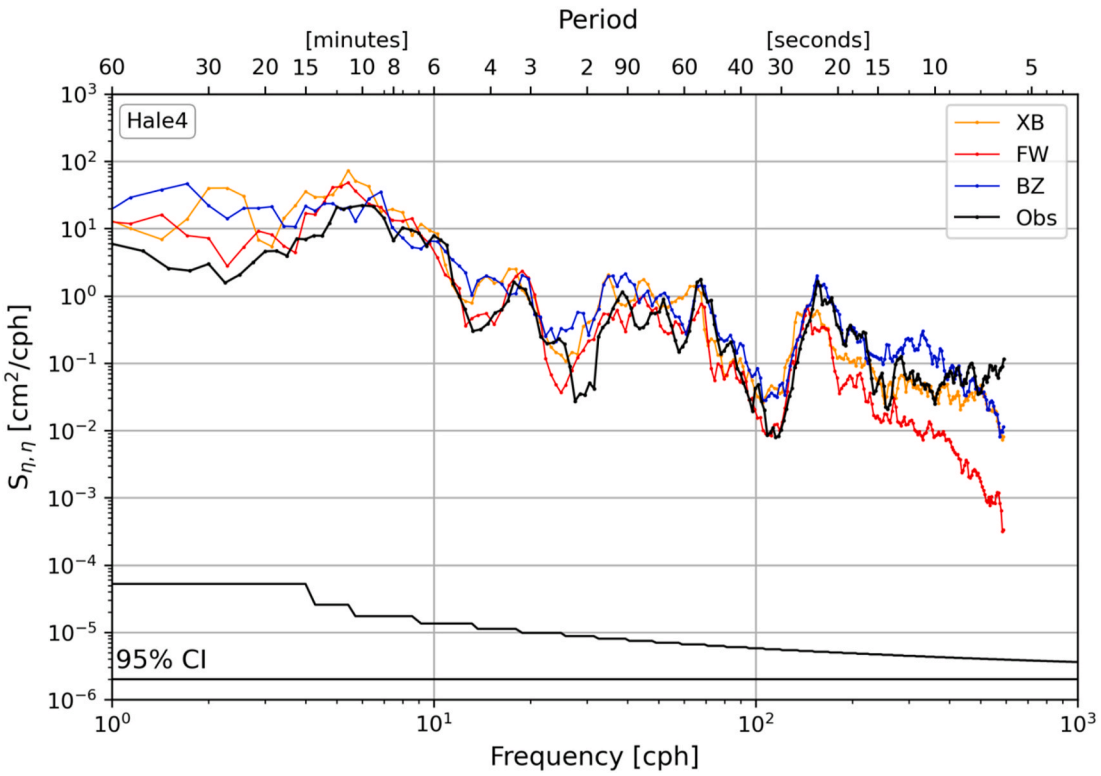

Fig. 4. Power spectral density of observed sea level (black curve), and modeled sea level (BZ, blue curve; FW, red curve; XB, orange curve) at harbor site Hale4. The model results are from simulations using a 7 m × 7 m grid (simulation 1 in Table 1). The vertical distance between the black lines at the bottom represents the 95% confidence interval for independent spectrum estimates. Every other point is independent.

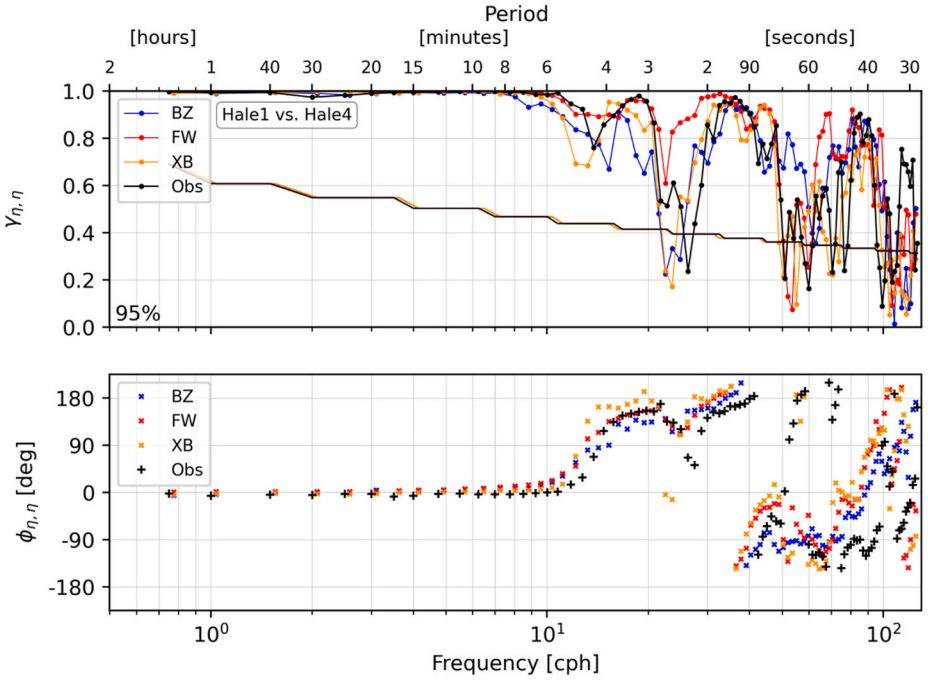

Fig. 5. Coherence amplitude (top panel), and coherence phase (bottom panel) of observed sea level (black curve), and modeled sea level (BZ, blue curve; FW, red curve; XB, orange curve) for harbor sites Hale1 versus Hale4. The model results are from simulations using a 7 m × 7 m grid (simulation 1 in Table 1). The black line in the coherence amplitude plot represents the 95% level of no significance. Every other point is independent.

and ~14 min. The peak at 50 s and a close-by peak at ~23 s (though not technically in the IG band) are relatively narrow band and significant features of the spectrum. Here, the spectra using time series from the three models contain highs and lows that are within an order of magnitude of the spectra from observations. At IG periods the models tend to overestimate the spectra from observations. At the short period portion of the spectra, XB overestimates the spectra of the observations at periods shorter than 15 s, and FW and BZ underestimate the spectra

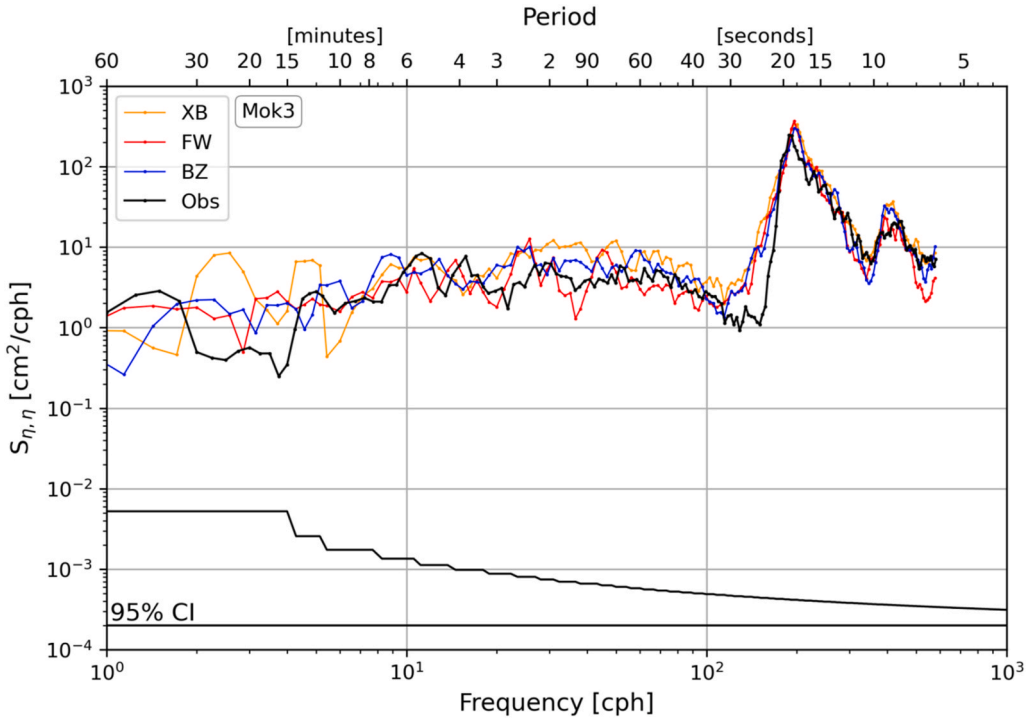

Fig. 6. Power spectral density of observed sea level (black curve), and modeled sea level (BZ, blue curve; FW, red curve; XB, orange curve) at coastal site Mok3 (12 m depth). The model results are from simulations using a 7 m × 7 m grid (simulation 2 in Table 1). The vertical distance between the black lines at the bottom represents the 95% confidence interval for independent spectrum estimates. Every other point is independent.

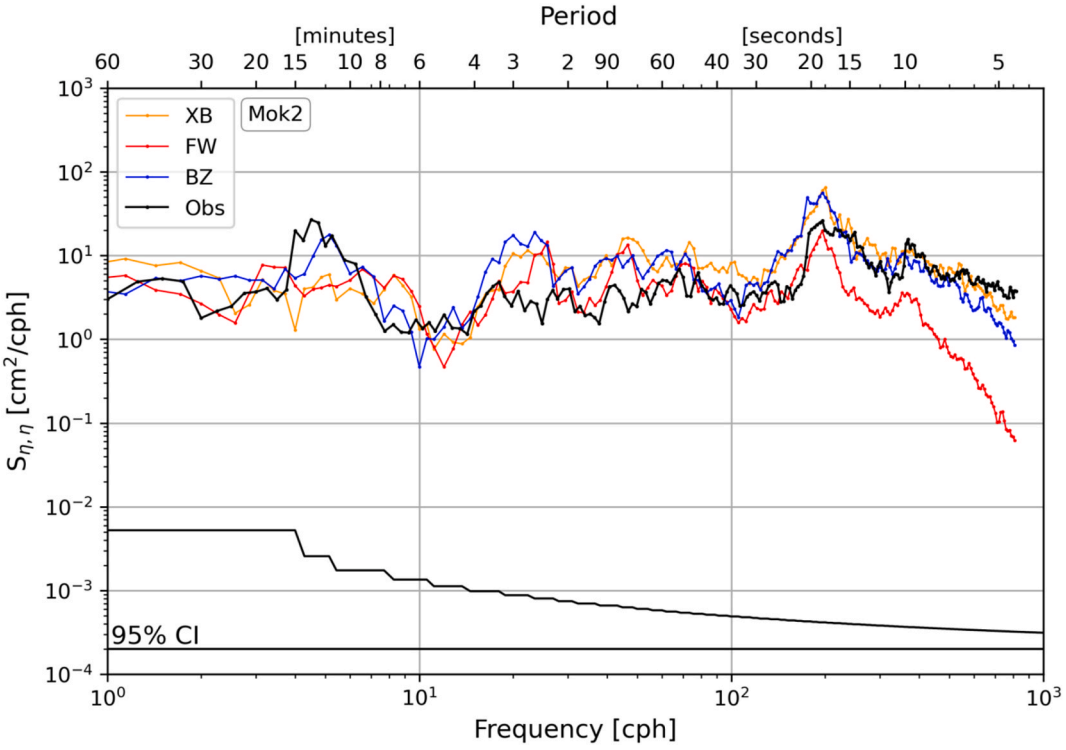

Fig. 7. Power spectral density of observed sea level (black curve), and modeled sea level (BZ, blue curve; FW, red curve; XB, orange curve) at coastal site Mok2 (6 m depth). The model results are from simulations using a 7 m × 7 m grid (simulation 2 in Table 1). The vertical distance between the black lines at the bottom represents the 95% confidence interval for independent spectrum estimates. Every other point is independent.

from observations at periods shorter than 10 s. All three models have dynamically transferred energy out of the incoming swell peak, and from periods of 10 s to 10 min those results are statistically consistent with the pressure record.

The coherence amplitude and phase for Mok3 versus Mok2 sites are shown in Fig. 9. We find that the coherence amplitude curves using

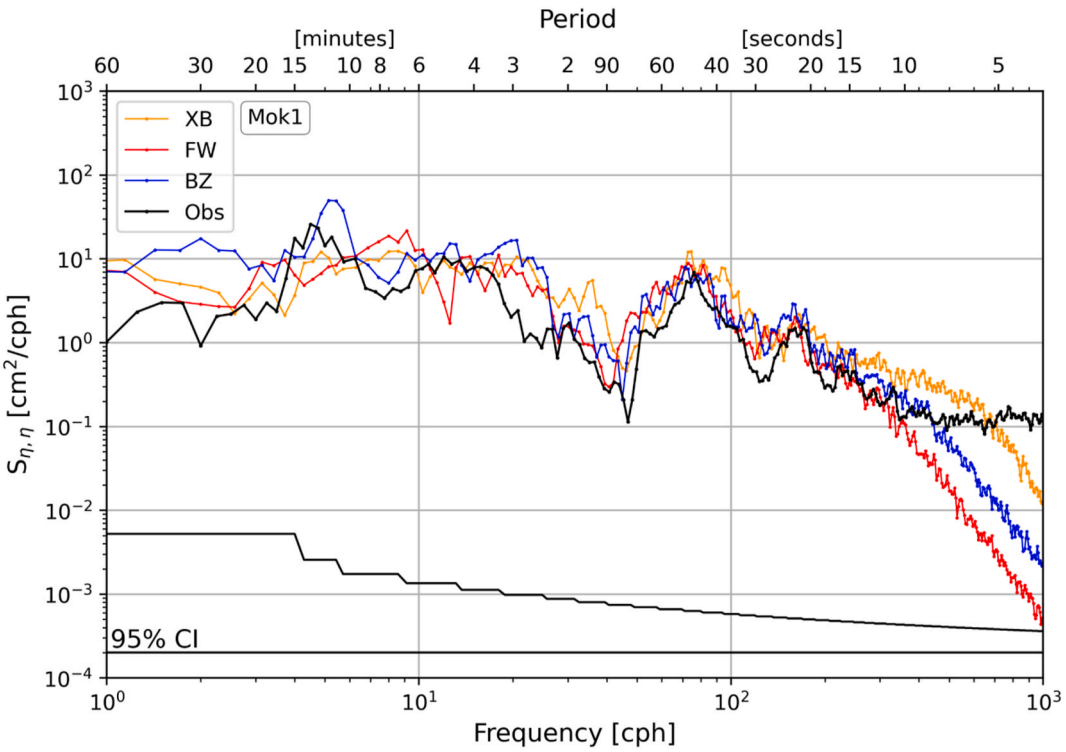

Fig. 8. Power spectral density of observed sea level (black curve), and modeled sea level (BZ, blue curve; FW, red curve; XB, orange curve) at coastal site Mok1 (2 m depth). The model results are from simulations using a 7 m × 7 m grid (simulation 2 in Table 1). The vertical distance between the black lines at the bottom represents the 95% confidence interval for independent spectrum estimates. Every other point is independent.

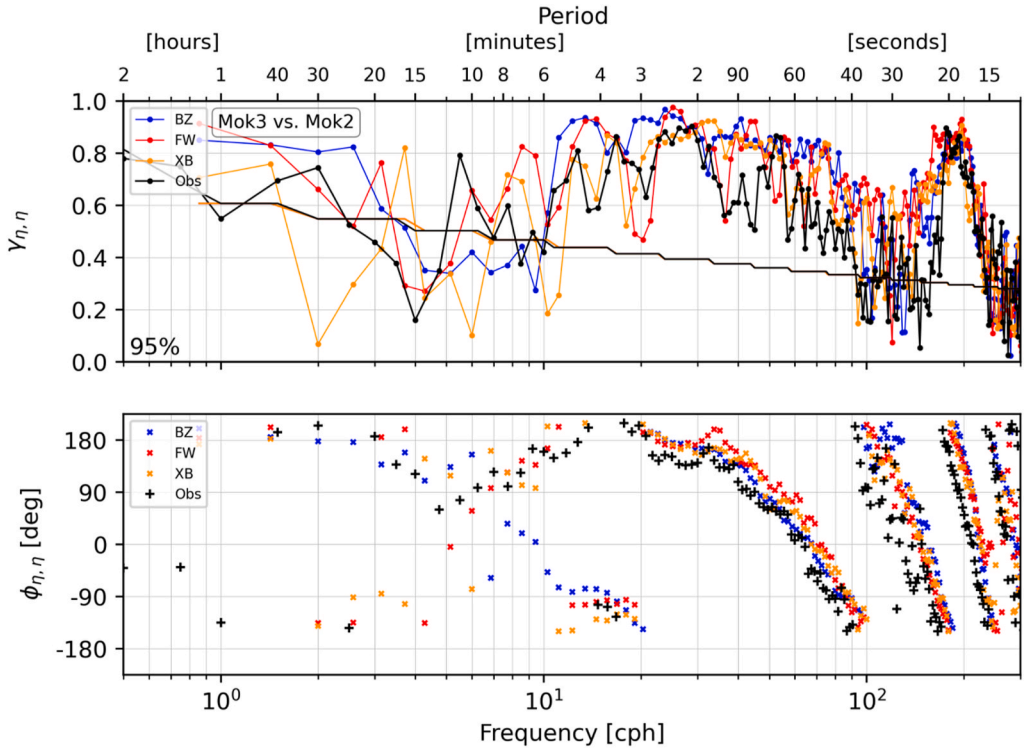

Fig. 9. Coherence amplitude (top panel), and coherence phase (bottom panel) of observed sea level (black curve), and modeled sea level (BZ, blue curve; FW, red curve; XB, orange curve) for Mokuleia sites Mok3 (12 m depth) versus Mok2 (6 m depth). The model results are from simulations using a 7 m × 7 m grid (simulation 2 in Table 1). The black line in the coherence amplitude plot represents the 95% level of no significance. Every other point is independent.

model outputs from the three models generally replicate the corresponding highs and lows seen in the coherence amplitude from observations. This result also holds for the coherence phase curves, and is especially evident at periods of 4 min and shorter where there is clear phase wrapping which indicates wave propagation.

In Fig. 10, the coherence amplitude and phase are plotted for Mok3 versus Mok1. Again, there is general agreement of the coherence amplitude structure between the three models and observations. On the other hand, the coherence phase curves indicate inconsistencies when compared to the corresponding observations in the ~100 s to ~4 min period band in which the coherence amplitude remains statistically significant. At periods where the coherence amplitude is below the 95% confidence level (e.g., periods shorter than ~72 s), the coherence phase is random as expected. Addressing such inconsistencies is an ongoing research topic. Avenues for improvement include increased bathymetric resolution and localized forcing along with a host of other small details.

Fig. 11 shows the normalized root-mean-square-error (RMSE, based on sea level power spectral density) of the models versus observations in various period bands (e.g., 7–20 s, 20–30 s, etc.) at the instrument locations. A smaller RMSE in a given period band translates into a better agreement between the spectra from the models and the observations. For example, at site Hale1 BZ has an RMSE of 0.025 in the 4–6 min period band, which is smaller than both FW and XB, hence showing a better capability of BZ to replicate the observations in this period band; in the 2–3 min period band the RMSE of BZ is 0.2, a larger value than the remaining models, and the RMSE of FW is the smallest one out of the three models. Over the reef (left column of Fig. 11), all models in general are resolving the shorter period motions more accurately than the longer periods. Additionally, the RMSE is increasing towards shore. The spectral mismatch seen in Figs. 7 and 8 for the 2–3 min band is now revealed in the error calculation as the least accurate periods for all three simulations over the reef. Excluding the swell band, the most accurate model results appear to be in the near IG band (0.5–2 min; with the exception of XB at 35 s in the nearshore). At both harbor sites (right column of Fig. 11) we also find that the shorter period motions have smaller RMSE values (with the exception of BZ at Hale4), and the trends of the RMSE curves at the two sites are qualitatively similar.

The significant wave height (Hs) as a function of wave period is shown in Fig. 12, for the models (XB, orange curves; FW, red curves; BZ, blue curves) and observations (black curves). When comparing the different panels in this figure, note that the vertical ranges are different. Here we see that overall (with a few exceptions, especially for FW), over the reef sites the models tend to overestimate Hs across the entire period range. Inside the harbor, overestimation of Hs is highest at the longer IG periods. Across all panels, the Hs values of FW are mostly lower than the Hs values of the other models, whereas the Hs values of XB are higher than the Hs values from the other models.

It is important to mention some of the factors that could influence the model solutions. First, a frequency cutoff of ~10 s was applied to the wavemakers in the present model runs; however, waves of periods shorter than 10 s can certainly be generated by non-linear interactions as the waves propagate towards shore, especially in the breaking zone. Second, the finite size of the computational domain has the potential to introduce artificial long period oscillations. Third, the limited run time of the simulations means that very long IG waves cannot be resolved. Furthermore, the models are forced with spectra that were taken from the nearest available buoy (Waimea Buoy, 200 m depth), which is not positioned at the offshore boundary of the computational domains. The overall spectral energy provided as input is likely slightly higher than what one would have measured in 80 m depth, meaning that it is possibly contributing to the mismatch seen in the spectral amplitudes of the models versus observations.

5.1.3. *Wavenumber-frequency spectra over the reef*

Following (Oltman-Shay and Guza (1987), we employed the Iterative Maximum Likelihood Estimate (IMLE) technique to reveal the frequency-wavenumber spectral energy content using outputs from the three models. As we do not have observations from an alongshore array,

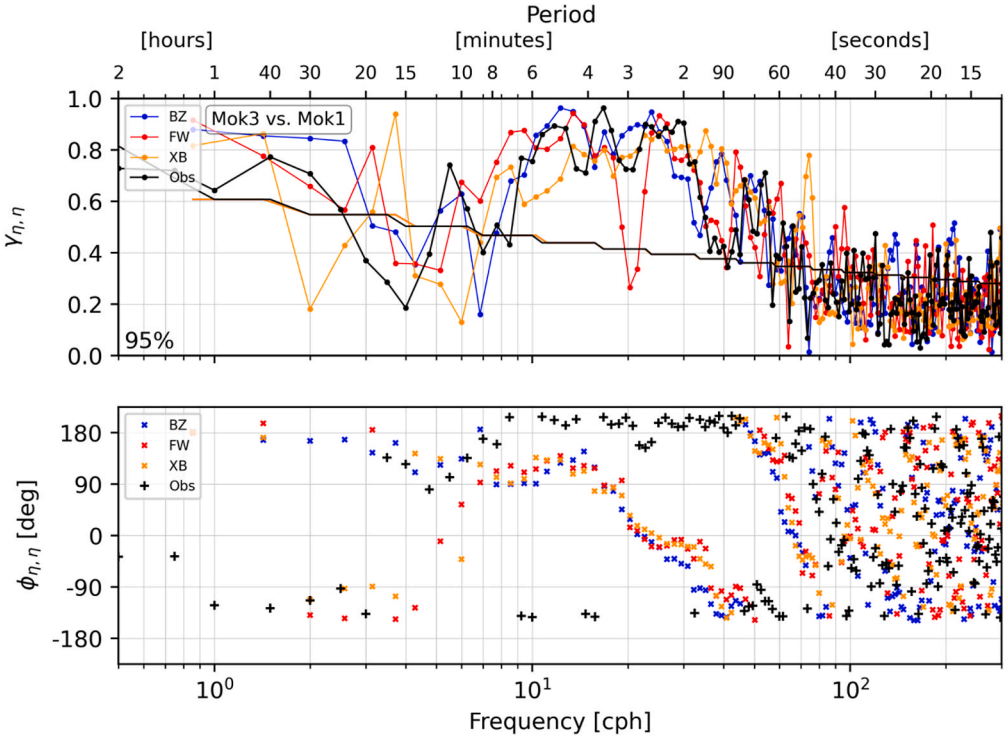

Fig. 10. Coherence amplitude (top panel), and coherence phase (bottom panel) of observed sea level (black curve), and modeled sea level (BZ, blue curve; FW, red curve; XB, orange curve) for Mokuleia sites Mok3 (12 m depth) versus Mok1 (2 m depth). The model results are from simulations using a 7 m × 7 m grid (simulation 2 in Table 1). The black line in the coherence amplitude plot represents the 95% level of no significance. Every other point is independent.

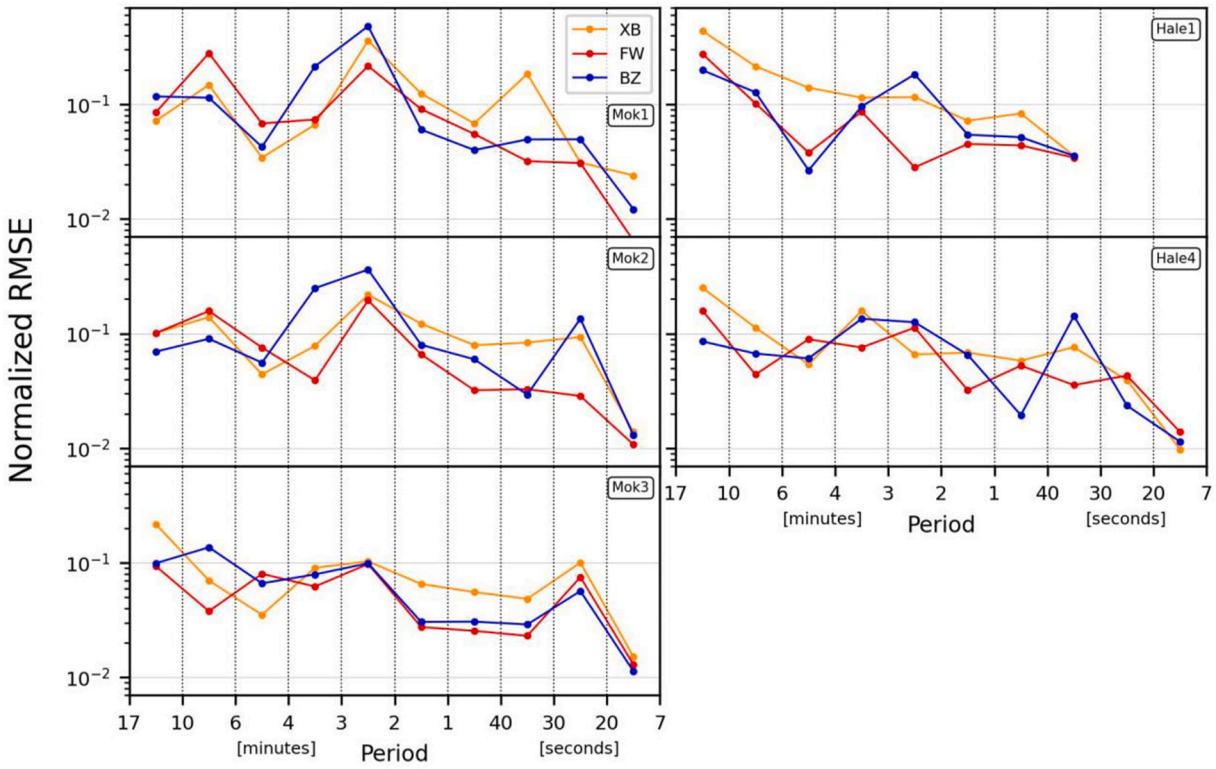

Fig. 11. Log of the normalized RMSE (based on sea level power spectral density) for the three models (XB, orange curves; FW, red curves; BZ, blue curves), as a function of period (in units of seconds and minutes), at the observational sites of Mokuleia (Mok1-Mok3) and Haleʻiwa Harbor (Hale1 and Hale4). The results correspond to data from simulation 1 (right column) and simulation 2 (left column) from Table 1. In the near IG band (30s to ~3min) FW and BZ are outperforming XB for all three reef locations.

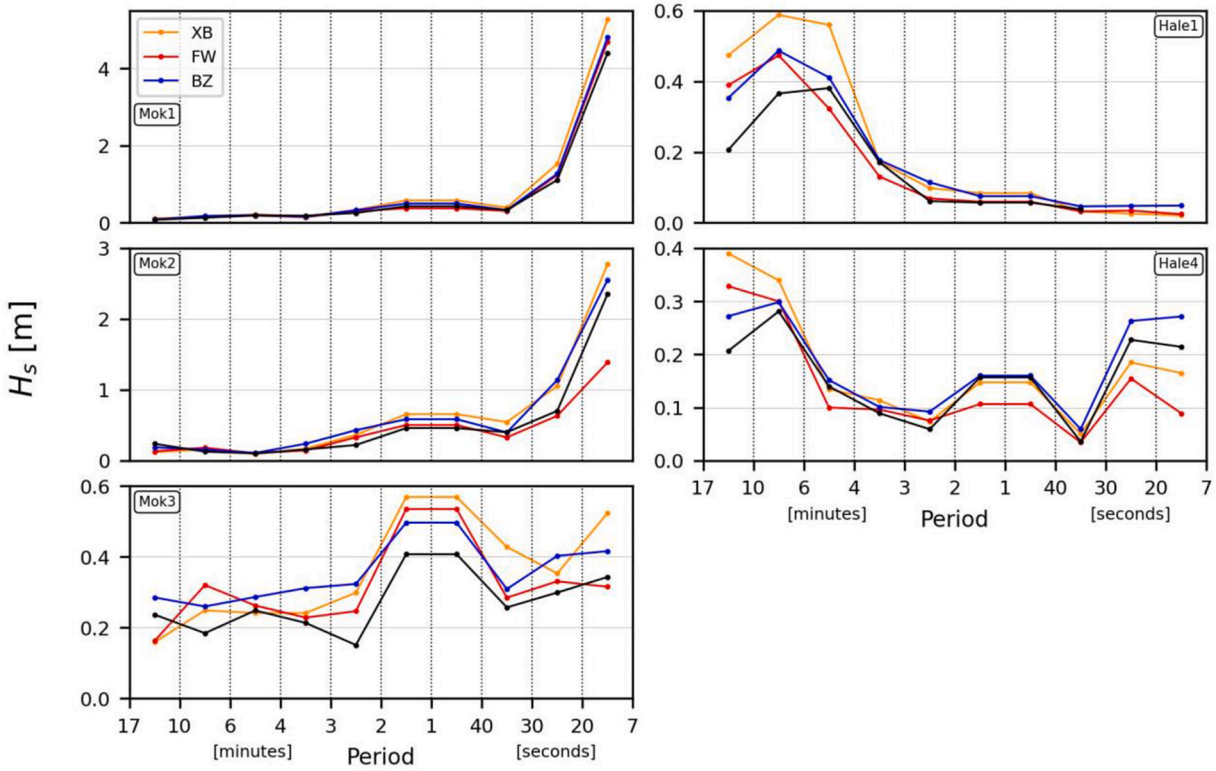

Fig. 12. Observed (black curves) and modeled (XB, orange curves; FW, red curves; BZ, blue curves) significant wave height (Hs) as a function of period (in units of seconds and minutes), at the observational sites of Mokuleia (Mok1-Mok3) and Haleʻiwa Harbor (Hale1 and Hale4). The results correspond to data from simulation 1 (right column) and simulation 2 (left column) from Table 1.

we designed a 550-m-long virtual array of six sites along the Mokuleia stretch of coastline where the coastline has minimal curvature (centered ~900 m east from the observational Mokuleia cross-shore array), and collected model data at those sites. We then compared the IMLE results of all three models against each other to check for the level of consistency among these models. In addition to the information that was extracted from auto- and cross-spectral analyses from the previous sections, an IMLE analysis may more clearly reveal: (i) the frequency bands and associated wavenumber ranges of most energetic wave motions; (ii) the dominant propagation direction (i.e., westward/eastward) in a certain frequency range; and (iii) the signature of edge wave modes and/or leaky waves (if those exist).

Our IMLE analysis resulted in the k-f spectra seen in Fig. 13. Calculations were made using data from simulation 2 (see Table 1). The rows correspond to results using data from each of the three models (see corresponding XB, FW, and BZ labels). The left column (panels a, c, and e) represents results using model data from the alongshore component of the velocity field, and the right column (panels b, d, and f) represents results using model data from the cross-shore component of the velocity field. Positive wavenumbers correspond to waves propagating eastward from Mokuleia (towards Hale'iwa Harbor), whereas negative wavenumbers correspond to waves propagating westward. The colorbar shows the percent of maximum power (for a given model, the power spectral density in each bin is normalized by its maximum power spectral density out of all bins). To see whether the spectra correspond to edge waves, we included the theoretical edge-wave dispersion curves for several low modes (n = 0, 1, 2, 3, 4), and a higher mode (n = 8). The theoretical leaky wave regime is contained within the two diagonal dashed curves. It is important to keep in mind that those dispersion curves were derived for an idealized scenario of a straight coastline, uniform cross-shore slope, and no alongshore slope; since most Hawai'i beaches do not fall into this category, it is not expected to obtain a good match with those curves even if such IG waves are dominant in our data. However, it is still interesting to see how the energy generated by the models is distributed in this k-f regime, relative to those theoretical curves.

All of the panels of Fig. 13 reveal elevated power levels in the positive half of the wavenumber regime, indicating eastward propagation of IG waves in the 0.5–2 min period band. At longer IG periods (lower portion of the plots), in some of the panels we see a mix of eastward plus slightly westward propagation (e.g., panels b and c). For the results of both the alongshore and cross-shore velocity components, the elevated power levels from all three models show up in the regime where the theory predicts high-mode edge waves and leaky waves. This is most clearly seen in the 0.5–2 min period band. Results that are qualitatively similar were obtained from the IMLE analysis of Su et al. (2021), which was done in a different reef environment. In Table 2 we provide the integrated percent of maximum power levels within the blue and green rectangles of Fig. 13. The blue rectangle lies in a k-f regime where high-mode ($n \geq 2$) edge waves and/or leaky waves may exist, and the green rectangle lies in a k-f regime where low-mode ($n \leq 1$) edge waves may exist. Using the values from Table 2 we can highlight and quantify a few similarities and differences that we identify from Fig. 13. In the IMLE results of the alongshore velocity component (Fig. 13, left

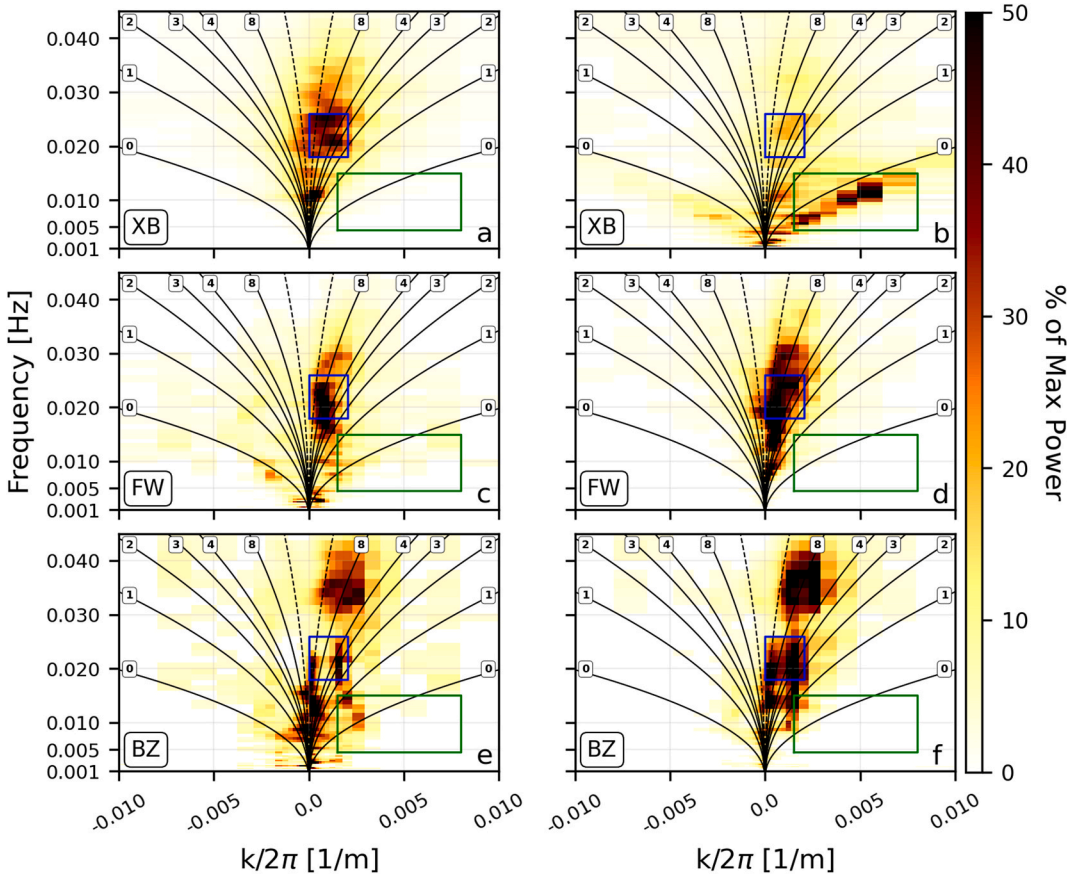

Fig. 13. Frequency-wavenumber spectra calculated using the Iterative Maximum Likelihood Estimate (IMLE) method. Colorbar is the percent of maximum power (for a given model, the power spectral density in each bin is normalized by the maximum power spectral density out of all bins). The calculations were made using data from simulation 2 (see Table 1) at an alongshore array of six gauges spanning 550 m-long and positioned 30 m from shore (centered ~900 m east from the observational Mokuleia cross-shore array). The left panel corresponds to the alongshore velocity data, and the right panel to the cross-shore velocity data. The theoretical edge wave curves are plotted and labeled for modes 0–4, and 8, for eastward propagation (right half), and westward propagation (left half). A quantitative comparison of the integrated percent max power is provided in the text for the green and blue rectangles.

Table 2
Cumulative Percent Maximum Power (Pcum) and percent difference (% diff; relative to the largest value out of the three models; largest value is highlighted in bold), from IMLE analysis using alongshore and cross-shore velocity components from the model outputs, at selected k-f regimes.

	Alongshore				Cross-shore			
	Blue		Green		Blue		Green	
	P_{cum}	% diff	P_{cum}	% diff	P_{cum}	% diff	P_{cum}	% diff
XB	**34.7**	–	3.1	74.9	14.0	71.1	**23.7**	–
FW	31.4	9.4	10.4	17.2	**48.4**	–	2.6	89.0
BZ	24.2	30.0	**12.5**	–	38.9	19.6	8.9	62.4

column), XB and FW seem to have a stronger signature of leaky and/or high-mode edge waves than BZ has (blue rectangles), and BZ has a stronger signature of low-mode edge waves than the other models have (green rectangles). As for the IMLE results of the cross-shore velocity component (Fig. 13, right column), BZ and FW have much stronger signature in the leaky and/or high-mode edge wave regime, than XB has, whereas XB has a much stronger signature of low-mode edge waves (i.e., FW and BZ are lower with 89% and 62.4% percent difference, respectively). The above indicate that, although the three models are consistent in simulating westward-propagating IG waves, the proportion of low-mode edge waves, high-mode edge waves, and leaky waves, is somewhat inconsistent among the models. The difference between the dispersion properties of the Boussinesq models versus the non-hydrostatic model may be responsible for those inconsistencies. One attempt to reduce dispersion errors was done by de Ridder et al. (2021), who implemented a two-layer non-hydrostatic version of XB. That possibility, and others, may be examined in a separate effort involving a different set of analyses.

5.2. Model energetics: 2D spectral distribution

The model outputs from simulation 4 (see Table 1) were used to create 2D maps to reveal the spatial distribution of power spectral density (PSD) in the following period bands: 5–30 s, 0.5–1 min, 1–2 min, 2–4 min, 4–8 min, and 8–17 min. In Figs. 14 and 15 we compare the maps of the three models: XBeach (XB), FUNWAVE (FW), and BOSZ (BZ), for the SS band and 0.5–1 min IG band. Figures S3-S6 of the supporting information document provide the corresponding maps for the remaining IG period bands. In the SS band (Fig. 14), the spatial distribution of PSD is consistent among BZ and FW, whereas in XB we see higher PSD levels closer to shore along the entire coastline. In the 0.5–1 min IG band (Fig. 15), the PSD distribution is consistent among all three models. In all models we find that the highest spectral amplitudes in the cross-shore are confined between a short distance from shore and the ~20 m depth contour. In the alongshore, all models simulate a well-defined minima at the three channels where the water is deep and waves do not break (i.e., we see smaller spectral amplitudes of IG waves there). For the remaining IG bands (Figures S3-S6), the 2D spectral distribution of the three models is qualitatively the same (i.e., the regions of highs and lows are spatially consistent, but we clearly see differences in amplitudes). The three models produce what appears to be Laguerre-like standing wave patterns (e.g., Eckart, 1951) in the cross-shore along various segments of the coastline, especially where the coastline is uniform (this is most clearly seen in the 1–8 min period range).

The Laguerre-like standing wave patterns are better visualized by looking at cross section profiles that extend offshore from the shoreline. Since the three Mokuleia instrument locations lie in a cross-shore line, model data from a cross-shore profile overlapping with those three sites, plus 10 profiles from each side (21 profiles in total), was recorded for analysis. Two different sets of those profiles are shown in panels a and b of Figs. 16 and 17. The instrument locations are marked with magenta circles in panel a and magenta crosses in panel b. As seen in panel b, the

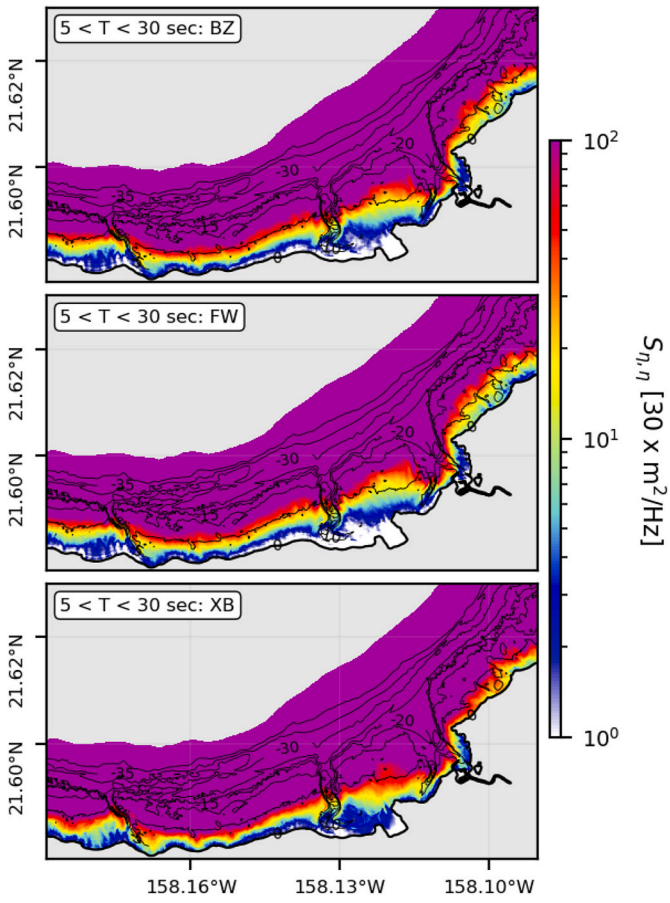

Fig. 14. Spatial distribution of sea level power spectral density in the 5–30 s period band, using modeled sea level data from simulation 2. From top to bottom, the panels correspond to: (a) BOSZ (BZ); (b) FUNWAVE (FW); and (c) XBeach (XB).

10 profiles west of the observations have a steep reef-edge, whereas the 10 profiles to the east have a much more moderate reef-edge slope (in that figure, we differentiate those by the solid and dashed gray lines, respectively).

In Figs. 16 and 17, rows 2–4 correspond to different period bands (see legends), panels c, e, and g (left column) are PSD maps of different period bands (only results from the BOSZ model are shown here), and panels d, f, and h (right column) show the corresponding averaged cross-shore profiles from the three models (dashed/solid curves correspond to the 10 profiles east/west from the three observational sites). In panels d, f, and h, we also superimposed the corresponding observed spectral amplitudes plus their uncertainties (magenta circles with error bars).

5.2.1. SS band 5–30 s (Fig. 16, panels c & d)

The high spectral levels offshore are decaying towards the shore. The rapid decay just shoreward of the 12 m observational site (Mok3) indicates the region where SS wave breaking takes place. When compared to the observations (see magenta symbols), the spectra from all three models indicate a consistent decrease in spectral levels towards shore. All models are overestimating the spectral levels at the 12 m site, and FW and BZ are in good agreement with the observations at the shallower sites. XB overestimates the spectra offshore and over the reef, except for within the 200 m nearest to shore. We also note that there is a significant difference in spectral amplitudes between the steep-type (solid curves) and more moderate-type (dashed curves) bathymetric profiles. This strong sensitivity to bathymetric profile is specific for the Mokuleia domain shown here, and it may be even more dramatic elsewhere along the coast.

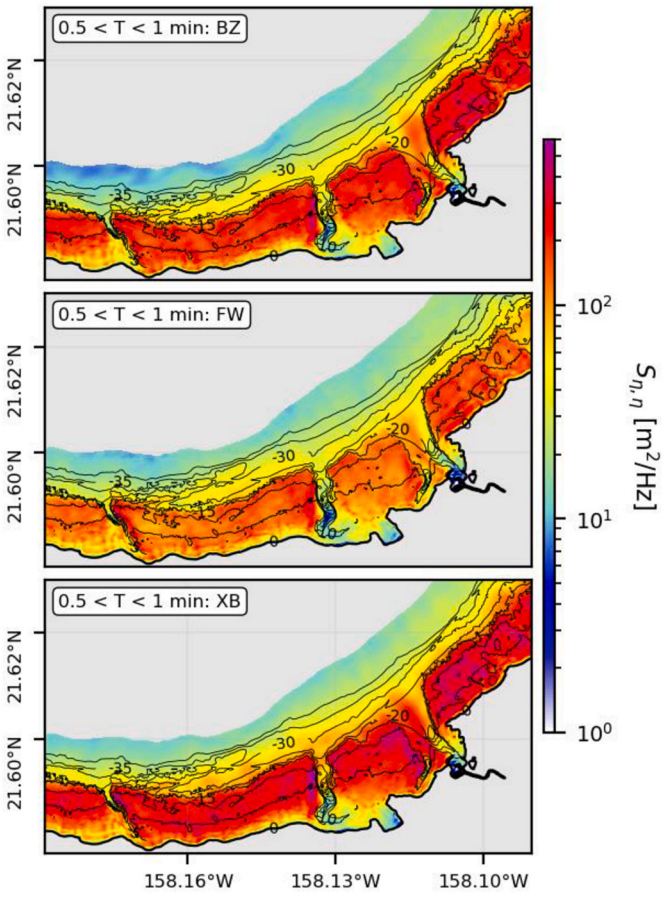

Fig. 15. Spatial distribution of sea level power spectral density in the 0.5–1 min period band, using modeled sea level data from simulation 2. From top to bottom, the panels correspond to: (a) BOSZ (BZ); (b) FUNWAVE (FW); and (c) XBeach (XB).

We calculated the ratio of integrated SS energy nearshore (between 0.3 km and 0.5 km from shore) and offshore (between 1.1 km and 1.3 km from shore), as a proxy for how much SS energy has dissipated in each model between the offshore and nearshore regimes for each of the beach profiles (steep versus moderate). For the steep profile, we obtained the following ratios (in terms of percent): 27.9%, 9.4%, and 10.8%, for XB, FW and BZ. For the moderate profile, we obtained the following ratios (in terms of percent): 25.6%, 10.9%, and 12.1%. We learned two things from these results: (i) in FW and BZ the dissipation is qualitatively the same (around ~90% dissipation), higher than the dissipation in XB (around 70% dissipation); (ii) for a given model, the ratios are qualitatively the same for both the steep and moderate types of beach profiles (within 1~3%).

5.2.2. IG band 0.5–1 min (Fig. 16, panels e & f)

These results show the coastal response of our shortest IG band. We have a maximum at the coast, followed by several maxima going offshore (specifically, a total of 4–5 maxima from the shoreline to the reef-edge, as seen in panel f). The offshore-most maximum occurs at the reef-edge (located ~900 m from shore; see panel b). Although the cross-shore PSD structure of all three models is qualitatively the same, FW and BZ produce the best agreement with observations at the three reef sites, and XB significantly overestimates the spectral amplitudes over the entire reef, except for the 100 m nearest to shore where all models are in agreement. The difference in spectral amplitudes of the steep-type (solid curves) and the moderate-type (dashed curves) beach profiles, is much smaller here as compared to what we see in the SS band. The cross-shore standing wave pattern seen here resembles the theoretical structure predicted for edge waves along a uniform coastline with a beach of constant slope. According to that theory, those waves obey a dispersion relation that permits a discrete number of frequencies and associated wavenumbers, and the standing wave patterns follow Laguerre polynomials (Eckart, 1951). Those cross-shore standing wave patterns were investigated in more detail by Azouri (2016), who showed that they result from a superposition of free edge and leaky waves that dominate the IG energy in the surf zone. Outside the surf zone, he found that bound wave energy dominates the IG wave field under strong SS forcing conditions.

5.2.3. IG band 1–2 min (Fig. 16, panels g & h)

The results here are similar to the ones from panels e & f, except that the cross-shore separation between the maxima has increased, resulting in one less maximum (a total of 3–4). At the shallowest site all models overestimate the PSD from observations. At the 12 m site, the PSDs of all models overlap with the error bars of the observed spectra, and at the intermediate site only FW is within the error bars of the PSD from observations.

5.2.4. IG bands longer than 2 min (Fig. 17, panels c & d, e & f, and g & h)

We identify a further increase in the separation between adjacent maxima, as well as a decrease in the total number of maxima that fit over the reef. The best agreement with observations that we see here is in the 4–8 min period band where the three models fall within the error bars of the observations.

These spectral maps show that the three models simulate a complex 2D structure that, at certain IG bands (in particular, the 1–8 min band) is dominated by cross-shore structure of peaks and valleys in between the shoreline and the reef-edge. In the alongshore, the structure is more uniform except for where there are channels.

6. Discussion

Our results indicate that the three models simulate gravity and infragravity wave dynamics that are qualitatively consistent with sea level observations over the reef and inside the harbor within the frequency bands that are applicable for our research. The models qualitatively reproduce the observed levels of spectral amplitude and shape of various peaks and valleys that are narrow-banded inside the harbor and broad-banded over the reef. Our analyses also reveal that the models can reproduce the horizontal structures that correspond to the potentially-resonant oscillations inside the harbor. Over the reef, the models can reproduce the observed wavenumber content in the cross-shore, except within the surf zone where in certain frequency bands the modeled coherence phases do not agree well with observations. Although observations were not available for an analysis of the alongshore wavenumber content, we verified the data from the models by comparing the model frequency-wavenumber spectra against each other. The IG wave fields generated by the three models point to dominance of high-mode edge waves and/or leaky waves with propagation that is predominantly from west to east at the Mokuleia observation site.

Although the selected phase-resolving models replicate realistic gravity and IG wave fields within the computational domains that were considered in this study, it is important to understand their limitations, such as: (i) a portion of the high-frequency content that is provided to the wavemakers of these models is excluded in order to satisfy the underlying assumptions of the model formulations; and (ii) for a given domain, excitation of waves having wavelengths on the order of the domain's dimensions may result in dominant spectral amplitudes which may require establishing a low-frequency cutoff. Other limitations arise from the strong dependency of the models on the quality of the input that is provided to them; for instance: (i) the bathymetry dataset used in this study was created by blending several datasets of varying grid resolutions that were collected during different times (during which the shoreline may have changed as a result of high wave action and erosion);

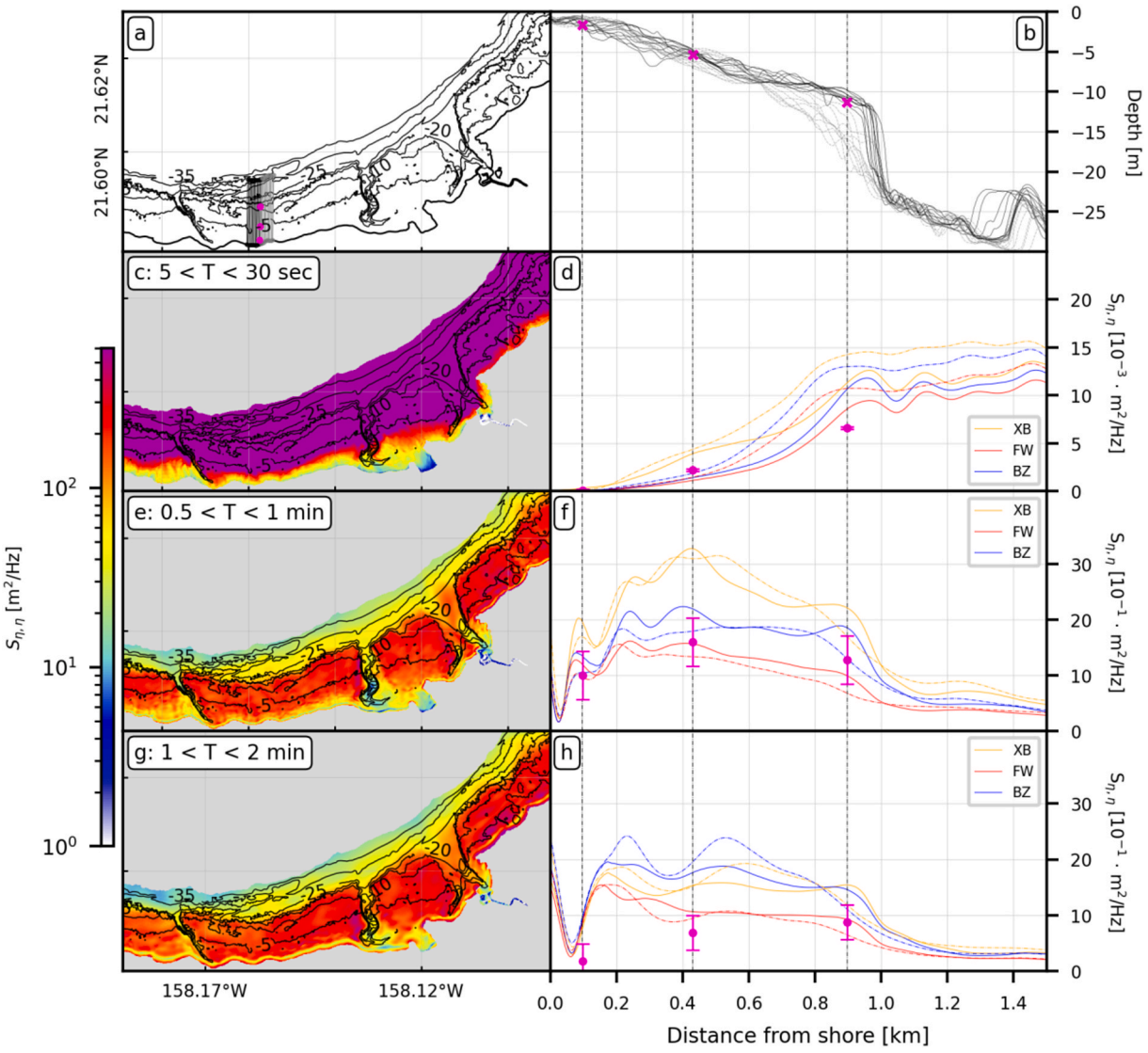

Fig. 16. (a) Contour map of the nearshore portion of our computational domain with the 21 cross-shore lines and 3 observational sites at Mokuleia (Mok1-Mok3, magenta circles). (b) Beach profiles of the 21 lines from panel a (solid/dashed gray correspond to steep/moderate profiles). Rows 2–4 contain maps of PSD (left column), and average PSDs of the cross-shore profiles (right column), in the 5–30 s (panels c–d), 0.5–1 min (panels e–f), and 1–2 min (panels g–h) period bands. In panels d, f and h, the solid/dashed lines are averages of the profiles with steep (black) and moderate (gray) reef-edge slopes from panel b. The observational PSDs and corresponding standard deviations in panels d, f and h, are shown in magenta. These results correspond to simulation 2 from Table 1.

and (ii) the directional spectra provided to the wavemaker may not be representative of spectra that would be observed at the offshore boundary.

7. Conclusion

Three 2DH phase-resolving nearshore wave models were tested in conjunction with multiple pressure gauge observations to examine their performance and the similarities/differences among them. The intended application is to accurately simulate runup and inundation at fringing reefs or mixed reef/sloping beach coastlines, including structures such as harbors. In the Hawaiian archipelago there are many socioeconomic nearshore environments that have such features. For the model comparisons, Oahu's North Shore was selected due to the availability of data, both in-situ pressure and high resolution bathymetry. All three models were capable of transferring incoming SS energy into short and long period IG waves plus higher frequency swell waves/bores, and consistent results among the models were found over the reef and inside the harbor.

The investigated models are capable of being employed in the nearshore to simulate wave transformation processes under real-world scenarios. Specific applications to a particular coastline may favor one model over the other, or the need for additional features not tested here. In the course of executing the NOAA Coastal Resilience grant "*Enhanced Community Resilience With Real-Time Notifications of Hazardous Wave-Driven Flooding and Erosion Events*", the BOSZ model was employed to create a live 6-day run-up forecast ("*Wave Run-Up Forecast: West Maui*") and a long-term wave-driven flooding tool ("*Sea Level Rise: West Maui Wave-Driven Flooding With Sea Level Rise*"). These products are available at *PacIOOS (*www.pacioos.org*)* and will be extended to other locations in the future. We conclude that each of the models tested here could potentially be used for such coastal wave forecasting applications.

CRediT authorship contribution statement

Assaf Azouri: Writing – original draft, Visualization, Software, Methodology, Data curation. **Volker Roeber:** Writing – review & editing, Software, Methodology, Conceptualization. **Martin D. Guiles:**

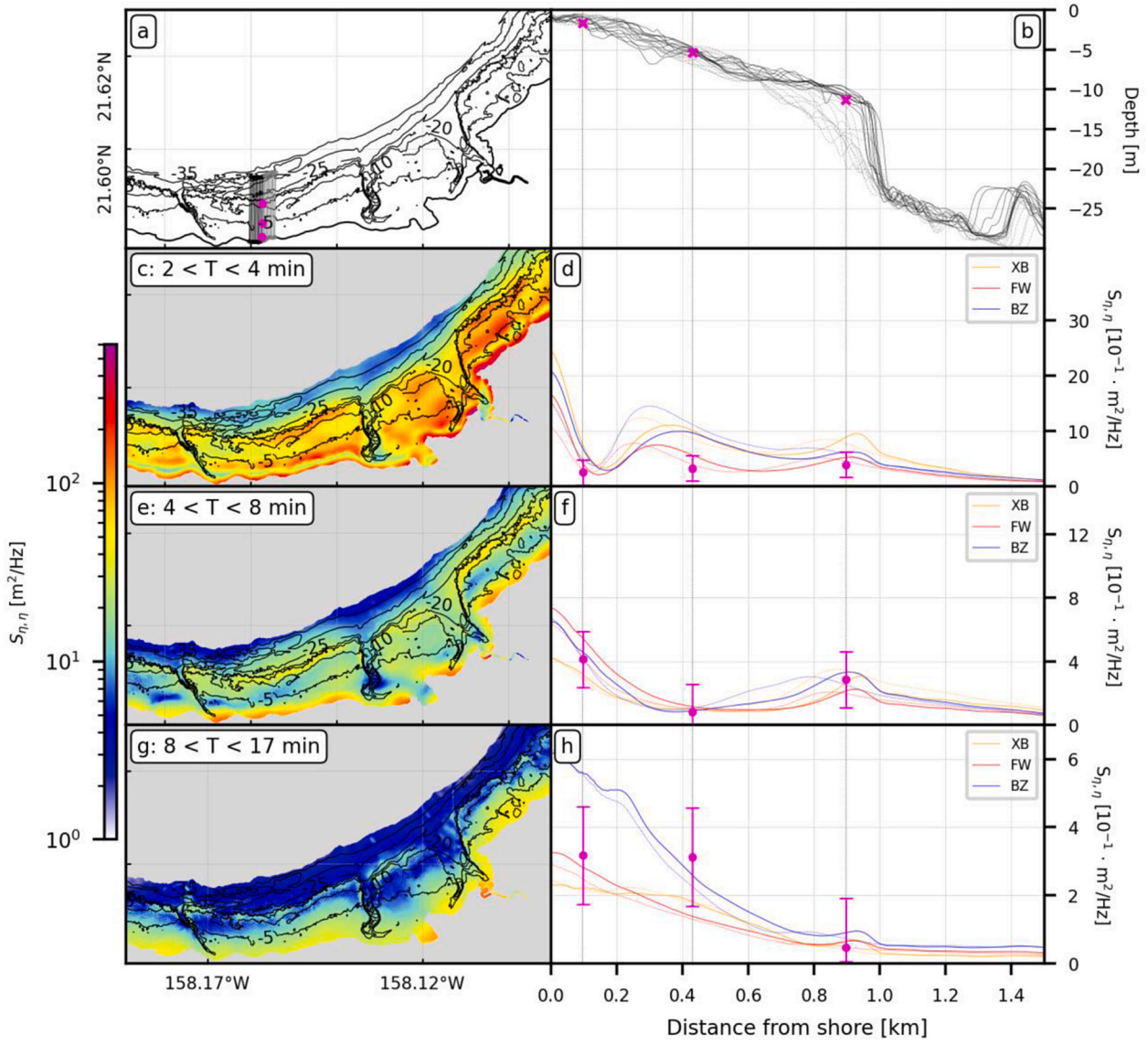

Fig. 17. (a) Contour map of the nearshore portion of our computational domain with the 21 cross-shore lines and 3 observational sites at Mokuleia (Mok1-Mok3, magenta circles). (b) Beach profiles of the 21 lines from panel a (solid/dashed gray correspond to steep/moderate profiles). Rows 2–4 contain maps of PSD (left column), and average PSDs of the cross-shore profiles (right column), in the 2–4 min (panels c–d), 4–8 min (panels e–f), and 8–17 min (panels g–h) period bands. In panels d, f and h, the solid/dashed lines are averages of the profiles with steep (black) and moderate (gray) reef-edge slopes from panel b. The observational PSDs and corresponding standard deviations in panels d, f and h, are shown in magenta. These results correspond to simulation 2 from Table 1.

Writing – review & editing, Software, Methodology. **Mark Merrifield:** Writing – review & editing, Data curation. **Janet Becker:** Writing – review & editing, Data curation. **Douglas S. Luther:** Conceptualization, Methodology, Writing, Review & Editing, Funding acquisition, Project guidance and management.

Declaration of competing interest

The authors declare that they have no known competing financial interests or personal relationships that could have appeared to influence the work reported in this paper.

Data availability

Data will be made available on request.

Acknowledgements

This work was funded by the National Oceanic and Atmospheric Administration (NOAA) grant "*Enhanced Community Resilience With Real-Time Notifications of Hazardous Wave-Driven Flooding and Erosion Events*" (award #NA17NOS4730143). *PACIOOS* is funded *in part by National Oceanic and Atmospheric Administration (NOAA)* Awards *#NA16NOS0120024 and #NA21NOS0120091)*. Volker Roeber acknowledges financial support from the I-SITE program Energy & Environment Solutions (E2S), the Communauté d'Agglomération Pays Basque (CAPB), and the Communauté Région Nouvelle Aquitaine (CRNA) for the chair position HPC-Waves and for supporting the KOSTARISK Laboratoire Commun.

Appendix A. Supplementary data

Supplementary data to this article can be found online at https://doi.org/10.1016/j.coastaleng.2024.104625.

References

Almström, B., Roelvink, D., Larson, M., 2021. Predicting ship waves in sheltered waterways–an application of xbeach to the stockholm archipelago, Sweden. Coast Eng. 170, 104026. https://doi.org/10.1016/j.coastaleng.2021.104026.

Azouri, A., 2016. Observations, forecast, and modeling of 0.5-200 min infragravity oscillations in Hale'iwa harbor region, Hawai'i (Doctoral dissertation, [Honolulu]: [University of Hawai'i at Mānoa],[December 2016]). http://hdl.handle.net/10125/51585.

Azouri, A., Roeber, V., Luther, D.S., 2018. The response of harbor environments protected by irregular fringing reef systems to strong gravity wave forcing - a case study. Coast. Eng. Proc. 1 (36).

Bellafont, F., Morichon, D., Roeber, V., Andre, G., Abadie, S., 2018. Infragravity period oscillations in a channel harbor near a river mouth. Coast. Eng. Proc. 1.

Bondehagen, A., Roeber, V., Kalisch, H., Buckley, M.P., Streßer, M., Cysewski, M., Horstmann, J., Bjørnestad, M., Ige, O.E., Frøysa, H.G., Carrasco-Alvarez, R., 2024. Wave-driven current and vortex patterns at an open beach: insights from phase-resolving numerical computations and Lagrangian measurements. Coast. Eng. 193, 104591.

Bretschneider, C.L., Kroc, H.J., Nakazaki, E., Casciano, F.M.m, 1986. Roughness of Typical Hawaiian Terrain for Tsunami Run-Up Calculations: a User's Manual. J.K.K. Look Laboratory Report. University of Hawai'i, Honolulu, HI.

Chen, Q., 2006. Fully nonlinear Boussinesq-type equations for waves and currents over porous beds. J. Eng. Mech. 132 (2), 220–230.

Cheung, K.F., Bai, Y., Yamazaki, Y., 2013. Surges around the Hawaiian Islands from the 2011 Tohoku tsunami. J. Geophys. Res.: Oceans 118 (10), 5703–5719.

Choi, J., Kirby, J.T., Yoon, S.B., 2015. Boussinesq modeling of longshore currents in the SandyDuck experiment under directional random wave conditions. Coast Eng. 101, 17–34.

Coastal Data Information Program (CDIP), McManus, M.A., Merrifield, M.A., Pacific Islands Ocean Observing System (PacIOOS), 2001. PacIOOS Wave Buoy 106: Waimea Bay, Oahu, Hawaii. Distributed by the Coastal Data Information Program (CDIP).

David, C.G., Roeber, V., Goseberg, N., Schlurmann, T., 2017. Generation and propagation of ship-borne waves-Solutions from a Boussinesq-type model. Coast Eng. 127, 170–187. https://www.researchgate.net/publication/318495516_Generation_and_propagation_of_ship-borne_waves_-_Solutions_from_a_Boussinesq-type_model.

David, C.G., Hennig, A., Ratter, B.M., Roeber, V., Zahid, Schlurmann, T., 2021. Considering socio-political framings when analyzing coastal climate change effects can prevent maldevelopment on small islands. Nat. Commun. 12 (1), 5882. https://www.researchgate.net/publication/355123089_Considering_socio-political_framings_when_analyzing_coastal_climate_change_effects_can_prevent_maldevelopment_on_small_islands.

de Ridder, M.P., Smit, P.B., van Dongeren, A.R., McCall, R.T., Nederhoff, K., Reniers, A. J., 2021. Efficient two-layer non-hydrostatic wave model with accurate dispersive behaviour. Coast Eng. 164, 103808.

Eckart, C., 1951. Surface Waves on Water of Variable Depth. Wave Report Nr. 100. SIO reference 51-12.

Elsayed, S.M., Gijsman, R., Schlurmann, T., Goseberg, N., 2022. Nonhydrostatic numerical modeling of fixed and mobile barred beaches: limitations of depth-averaged wave resolving models around sandbars. J. Waterw. Port, Coast. Ocean Eng. 148 (1), 04021045. https://doi.org/10.1061/(ASCE)WW.1943-5460.0000685.

Filipot, J.F., Guimaraes, P., Leckler, F., Hortsmann, J., Carrasco, R., Leroy, E., Fady, N., Accensi, M., Prevosto, M., Duarte, R., Roeber, V., 2019. La Jument lighthouse: a real-scale laboratory for the study of giant waves and their loading on marine structures. Philosophical Transactions of the Royal Society A 377 (2155), 20190008. https://doi.org/10.1098/rsta.2019.0008.

Grilli, S.T., Grosdidier, S., Guerin, C.-A., 2015a. Tsunami detection by high-frequency radar beyond the continental shelf. Pure Appl. Geophys. 173 (12), 3895–3934. https://link.springer.com/article/10.1007/s00024-015-1193-8.

Grilli, S.T., O'Reilly, C., Harris, J.C., Tajalli Bakhsh, T., Tehranirad, B., Banihashemi, S., Kirby, J.T., Shi, F., 2015b. Modeling of SMF tsunami hazard along the upper US East Coast: detailed impact around Ocean City, MD. Nat. Hazards 76, 705–746. https://doi.org/10.1007/s11069-014-1522-8.

Gruwez, V., Altomare, C., Suzuki, T., Streicher, M., Cappietti, L., Kortenhaus, A., Troch, P., 2020. An inter-model comparison for wave interactions with sea dikes on shallow foreshores. J. Mar. Sci. Eng. 8 (12), 985. https://doi.org/10.3390/jmse8120985.

Horillo, J., Grilli, S.T., Nicolsky, D., Roeber, V., Zhang, J., 2015. Performance benchmarking tsunami models for NTHMP's inundation mapping activities. Pure Appl. Geophys. 172, 869–884.

Kalisch, H., Lagona, F., Roeber, V., 2023. Sudden wave flooding on steep rock shores: a clear but hidden danger. Nat. Hazards 120, 3105–3125.

Larsen, J., Dancy, H., 1983. Open boundaries in short wave simulations - a new approach. Coast. Eng. 7, 285–297.

Lashley, C.H., Zanuttigh, B., Bricker, J.D., Van der Meer, J., Altomare, C., Suzuki, T., Roeber, V., Oosterlo, P., 2020. Benchmarking of numerical models for wave overtopping at dikes with shallow mildly sloping foreshores: accuracy versus speed. Environ. Model. Software 130, 104740.

Li, N., Roeber, V., Yamazaki, Y., Heitmann, T.W., Bai, Y., Cheung, K.F., 2014. Integration of coastal inundation modeling from storm tides to individual waves. Ocean Model. 83, 26–42.

Lynett, P.J., Gately, K., Wilson, R., Montoya, L., Arcas, D., Aytore, B., Bai, Y., Bricker, J. D., Castro, M.J., Cheung, K.F., David, C.G., 2017. Inter-model analysis of tsunami-induced coastal currents. Ocean Model. 114, 14–32.

Malej, M., Shi, F., Smith, J.M., 2019. Modeling Ship-Wake-Induced Sediment Transport and Morphological Change–Sediment Module in FUNWAVE-TVD. ERDC/CHL CHETN-VII-20. US Army Corps of Engineers, Vicksburg, MS. https://apps.dtic.mil/sti/pdfs/AD1074624.pdf.

Mancini, G., Briganti, R., McCall, R., Dodd, N., Zhu, F., 2021. Numerical modelling of intra-wave sediment transport on sandy beaches using a non-hydrostatic, wave-resolving model. Ocean Dynam. 71 (1), 1–20. https://link.springer.com/article/10.1007/s10236-020-01416-x.

Morichon, D., Roeber, V., Martin-Medina, M., Bellafont, F., Abadie, S., 2021. Tsunami impact on a detached breakwater: insights from two numerical models. J. Waterw. Port, Coast. Ocean Eng. 147 (2), 05021001.

Nwogu, O., 1993. Alternative form of Boussinesq equations for nearshore wave propagation. J. Waterw. Port, Coast. Ocean Eng. 119 (6), 618–638.

Oltman-Shay, Joan, Guza, R.T., 1987. Infragravity edge wave observations on two California beaches. J. Phys. Oceanogr. 17 (5), 644–663. https://doi.org/10.1175/1520-0485(1987)017<0644:IEWOOT>2.0.CO;2.

Pinault, J., Morichon, D., Roeber, V., 2020. Estimation of irregular wave runup on intermediate and reflective beaches using a phase-resolving numerical model. J. Mar. Sci. Eng. 8 (12). https://doi.org/10.3390/jmse8120993.

Pinault, J., Morichon, D., Delpey, M., Roeber, V., 2022. Field observations and numerical modeling of swash motions at an engineered embayed beach under moderate to energetic conditions. Estuar. Coast Shelf Sci. 279, 108143. https://www.sciencedirect.com/science/article/abs/pii/S0272771422004012?via%3Dihub.

Portland District Corps of Engineers, 2009. Condition Survey for Hale'iwa Small Boat Harbor. U. S. Army Corps of Engineers, Hydrographic Surveys.

Roeber, V., Bricker, J.D., 2015. Destructive tsunami-like wave generated by surf beat over a coral reef during Typhoon Haiyan. Nat. Commun. 6 (1), 1–9. https://www.nature.com/articles/ncomms8854.

Roeber, V., Cheung, K., 2012a. Bosz - Boussinesq ocean and surf zone model. NOAA, special report. Proceedings and Results of the 2011 NTHMP Model Benchmarking Workshop, Texas, Galveston, p. 437. In: https://nws.weather.gov/nthmp/documents/nthmpWorkshopProcMerged.pdf.

Roeber, V., Cheung, K., 2012b. Boussinesq-type model for energetic breaking waves infringing reef environments. Coast. Eng. 70, 1–20. https://www.researchgate.net/publication/257211433_Boussinesq-type_model_for_energetic_breaking_waves_in_fringing_reef_environment.

Roeber, V., Cheung, K., Kobayashi, M., 2010. Shock-capturing Boussinesq-type model for nearshore wave processes. Coast. Eng. 57, 407–423. In: https://www.researchgate.net/publication/257211050_Shock-capturing_Boussinesq-type_model_for_nearshore_wave_processes.

Roeber, V., Pinault, J., Morichon, D., Abadie, S., Azouri, A., Guiles, M., Luther, D., Delpey, M., Danglade, N., 2019. Improving wave run-up forecasts–benefits from phase-resolving models. Coastal Structures 2019, 752–761. https://core.ac.uk/download/pdf/347187864.pdf.

Roelvink, D., Reniers, A., Van Dongeren, A.P., De Vries, J.V.T., McCall, R., Lescinski, J., 2009. Modelling storm impacts on beaches, dunes and barrier islands. Coast. Eng. 56 (11–12), 1133–1152. https://svn.oss.deltares.nl/repos/openearthtools/sandbox/DSD_2014/Documents/Literature/Roelvink_et_al_2009.pdf.

Roelvink, D., McCall, R., Mehvar, S., Nederhoff, K., Dastgheib, A., 2018. Improving predictions of swash dynamics in XBeach: the role of groupiness and incident-band runup. Coast Eng. 134, 103–123. https://doi.org/10.1016/j.coastaleng.2017.07.004.

Sabatier, François, 2007. U.S. Army Corps of Engineers, coastal engineering manual (CEM), engineer manual 1110-2-1100. https://www.publications.usace.army.mil/USACE-Publications/Engineer-Manuals/.

Schnyder, J.S.D., Eberli, G.P., Kirby, J.T., Shi, F., Tehranirad, B., Mulder, T., Wintersteller, P., 2016. Tsunamis caused by submarine slope failures along western Great Bahama Bank. Sci. Rep. 6, 35925. https://doi.org/10.1038/srep35925.

Shelby, M., Grilli, S.T., Grilli, A.R., 2016. Tsunami hazard assessment in the Hudson River Estuary based on dynamic tsunami-tide simulations. Pure Appl. Geophys. 173, 3999–4037. https://doi.org/10.1007/s00024-016-1315-y.

Shi, F., Kirby, J.T., Harris, J.C., Geiman, J.D., Grilli, S.T., 2012. A high-order adaptive time-stepping TVD solver for Boussinesq modeling of breaking waves and coastal inundation. Ocean Model. 43, 36–51. https://personal.egr.uri.edu/grilli/shi_etal_om_2012.pdf.

Shi, F., Malej, M., Smith, J.M., Kirby, J.T., 2018. Breaking of ship bores in a Boussinesq-type ship-wake model. Coast Eng. https://doi.org/10.1016/j.coastaleng.2017.11.002. https://www.sciencedirect.com/science/article/abs/pii/S0378383917304246?via%3Dihub.

Smit, P.B., Stelling, G.S., Roelvink, D., van Thiel de Vries, J., McCall, R., Van Dongeren, A., Zwinkels, C., Jacobs, R., 2010. XBeach: Non-hydrostatic Model. Delft University of Technology and Deltares.

Su, F.-F., Ma, G., 2018. Modeling two-dimensional infragravity motions on a fringing reef. Ocean Eng. 153. https://doi.org/10.1016/j.oceaneng.2018.01.111. https://www.researchgate.net/publication/323663349_Modeling_two-dimensional_infragravity_motions_on_a_fringing_reef.

Su, S.F., Ma, G., Hsu, T.W., 2021. Numerical modeling of low-frequency waves on a reef island in the South China Sea during typhoon events. Coast Eng. 169, 103979.

Tehranirad, B., Kirby, J.T., Shi, F., 2016. Does morphological adjustment during tsunami inundation increase levels of hazard? Research report No.CACR-16-02. Center of Applied Coastal Research. Department of Civil and Environmental Engineering, University of Delaware. https://bpb-us-w2.wpmucdn.com/sites.udel.edu/dist/0/7241/files/2018/06/CACR-16-02-Tehranirad-etal_reduced-1nj2kpg.pdf.

Thompson, R.O., 1979. Coherence significance levels. J. Atmos. Sci. 36 (10), 2020–2021.

Thomson, R.E., Emery, W.J., 2014. Data Analysis Methods in Physical Oceanography. Newnes.

Tognacchini, C., 2022. Wave energy transformations in a complex reef environment; observations, modeling and applications (Masters thesis, [Honolulu]:[University of Hawai'i at Manoa],[December 2022]). https://hdl.handle.net/10125/105138.

Varing, A., Filipot, J.F., Delpey, M., Guitton, G., Collard, F., Platzer, P., Roeber, V., Morichon, D., 2021. Spatial distribution of wave energy over complex coastal bathymetries: development of methodologies for comparing modeled wave fields with satellite observations. Coast Eng. 169, 103793.

Watanabe, M., Goto, K., Roeber, V., Imamura, F., 2021. Identification of coastal sand deposits from tsunamis and storm waves based on numerical computations. J. Geophys. Res.: Earth Surf. 126 (7), 1–20. https://doi.org/10.1029/2021JF006092.

Watanabe, M., Yoshii, T., Roeber, V., Goto, K., Imamura, F., 2022. Derivation, validation, and numerical implementation of a two-dimensional boulder transport formulation by coastal waves. Journal of Earthquake and Tsunami 1–24. https://doi.org/10.1142/S179343112250018X.

Yamazaki, Y., Cheung, K.F., Kowalik, Z., 2011. Depth-integrated, non-hydrostatic model with grid nesting for tsunami generation, propagation, and run-up. Int. J. Numer. Methods Fluid. 67 (12), 2081–2107.

Zijlema, M., Stelling, G.S., Smit, P.B., 2011. SWASH: an operational public domain code for simulating wave fields and rapidly varied flows in coastal waters. Coast Eng. 58 (10), 992–1012. https://doi.org/10.1016/j.coastaleng.2011.05.015. https://swash.sourceforge.io/online_doc/swash.pdf.